https://doi.org/10.5194/essd-2025-728
Preprint. Discussion started: 26 January 2026

An operational global L-band soil moisture and vegetation optical depth dataset from optimized 40° SMOS brightness temperatures

Zanpin Xing[1,3,4], Xiaojun Li[*2,5], Frédéric Frappart[2], Gabrielle De Lannoy[6], Thomas Jagdhuber[7,8], Jian Peng[9,10], Lei Fan[11], Hongliang Ma[12], Karthikeyan Lanka[13,14], Xiangzhuo Liu[2], Mengjia Wang[2,15], Lin Zhao[16], Yongqin Liu[1,3,4], Jean-Pierre Wigneron[2]

[1]Center for Pan-third Pole Environment, Lanzhou University, Lanzhou, China

[2]INRAE, Bordeaux Sciences Agro, UMR 1391 ISPA, Villenave-d'Ornon, France

[3]Key Laboratory of Pan-third Pole Biogeochemical Cycling, Lanzhou, China

[4]Chayu integrated observation and research station of the Xizang Autonomous Region，Xizang, China

[5]Faculty of Geosciences and Engineering, Southwest Jiaotong University, Chengdu 611756, China

[6]Department of Earth and Environmental Sciences, KU Leuven, Heverlee B-3001, Belgium

[7]German Aerospace Center (DLR) Microwaves and Radar Institute Weßling, Germany

[8]Institute of Geography University of Augsburg (UniA) Augsburg, Germany

[9]Department of Remote Sensing, Helmholtz Centre for Environmental Research - UFZ, Leipzig, Germany

[10]Remote Sensing Centre for Earth System Research-RSC4Earth, Leipzig University, Leipzig, Germany

[11]Chongqing Jinfo Mountain Karst Ecosystem National Observation and Research Station, School of Geographical Sciences, Southwest University, Chongqing, China

[12]INRAE, UMR 1114 EMMAH, UMT CAPTE, Provence-Alpes-Cote d'Azur, F-84000 Avignon, France

[13]Centre of Studies in Resources Engineering, Indian Institute of Technology Bombay, Mumbai, India

[14]Centre for Climate Studies, Indian Institute of Technology Bombay, Mumbai, India

[15]School of Geo-Science and Technology, Zhengzhou University, Zhengzhou 450001, China

[16]School of Geographical Sciences, Nanjing University of Information Science & Technology, Nanjing 210044, China

Correspondence to: Xiaojun Li (xiaojunli_vod@163.com)

https://doi.org/10.5194/essd-2025-728
Preprint. Discussion started: 26 January 2026

Abstract. The Soil Moisture and Ocean Salinity (SMOS) mission delivers the first multi-angular L-band observations for retrieving global soil moisture (SM) and vegetation optical depth (VOD), two critical variables for understanding terrestrial water and carbon cycles. However, the combined effects of non-identical fields of view and aliasing in multi-angular SMOS brightness temperature (TB) observations can introduce noise and biases when the TBs are averaged to a nominal incidence angle, as done in the SMOS L3 dataset, thereby degrading land parameter retrievals. To address this issue, an optimized SMOS TB dataset was initially produced at a fixed 40° incidence angle, consistent with the Soil Moisture Active Passive (SMAP) mission. We then developed the first SMOS mono-angular SM and VOD products designed to achieve performance comparable to SMAP and improved relative to conventional multi-angle SMOS retrievals. The 40° TB optimization was performed using the L-band Microwave Emission of the Biosphere (L-MEB) model, and the inversion relied on the SMAP-INRAE-BORDEAUX (SMAP-IB) algorithm, yielding a global 40° SMOS TB record and associated SM and VOD products for 2010–2024 at 25 km spatial resolution, collectively referred to as SMOS-IB. Results showed that the optimized 40° TB reached a performance level comparable to SMAP and improved relative to SMOS-L3, both in its sensitivity to *in-situ* SM from the International Soil Moisture Network (ISMN) and in the reduction of global pixel-scale noise. When multiple evaluation metrics are considered, the SMOS-IB SM and VOD data, benefiting from the use of the optimized TB as input and a newly optimized soil roughness (Hr) parameterization, showed improved performance compared with those derived from SMOS L3 40° TB or from the multi-angular SMOS products. The SMOS-IB TB, SM and VOD products can be used for L-band algorithm development and SMAP harmonization, global drought monitoring, and studies of vegetation water and biomass dynamics. SMOS-IB is publicly available at https://zenodo.org/records/17647385 (Xing et al., 2025).

1 Introduction

Large-scale, long-term datasets of soil moisture (SM) and vegetation optical depth (VOD) provide the core information needed to investigate how terrestrial water and carbon systems function. Accurate satellite-derived SM estimates are essential for various research domains, including predicting agricultural yields, assessing flood and drought conditions, managing local water resources, and analyzing worldwide hydrological processes (Peng et al., 2021; Al Bitar et al., 2017; Sadri et al., 2020). Meanwhile, VOD, a vegetation index that gauges the extinction of microwave radiation by vegetation, is a valuable parameter for tracking vegetation water status (Zotta et al., 2024; Baur et al., 2024) and biomass information (Fan et al., 2022b; Li et al., 2025; Wigneron et al., 2024). Due to their deep penetration through vegetation canopies and elevated sensitivity to surface dielectric properties, L-band (~1.4 GHz) observations are widely considered as a preferred technique for large-scale monitoring of both SM and VOD. To date, the Soil Moisture and Ocean Salinity (SMOS) (Kerr et al., 2012; Wigneron et al., 2021) and Soil Moisture Active Passive (SMAP) (Entekhabi et al., 2010; O'neill et al., 2021), remain two main operational satellite missions providing global passive L-band brightness temperature (TB) observations dedicated to SM and VOD retrieval.

Although the main objective of both SMOS and SMAP missions is to retrieve SM, they are based on very different types of microwave technology. The SMAP mission, launched at the beginning of 2015, is the latest operational L-band satellite mission. It acquires mono-angular TBs at a fixed 40° incidence angle, encompassing both V- and H- polarization channels (Entekhabi et al., 2010). This mono-angular configuration makes it more difficult to derive SM and VOD simultaneously, as the potential information overlap between H- and V-polarized TB can result in an ill-posed inversion issue. To address this, SMAP retrieval algorithms are generally categorized into two types based on the polarization input: single-channel algorithms (SCA) and dual-channel algorithms (DCA). The SCA applies either H-polarization or V-polarization to estimate SM, while VOD is prescribed from external NDVI climatology (Jackson, 1993; Chan et al., 2016). On the contrary, DCA, which relies on both polarizations and enables the simultaneous retrieval of SM and VOD (O'neill et al., 2021), is increasingly interest in utilizing VOD for ecological applications, especially in monitoring vegetation dynamics (Frappart et al., 2020; Wang et al., 2024; Wigneron et al., 2024). Currently, several improved DCA approaches have been proposed, with their methodologies and performance comprehensively summarized and compared in (Gao et al., 2021). Among the available DCA-type retrieval products, a new mono-angular algorithm developed by INRAE Bordeaux (called SMAP-IB, hereafter referred to as IB_{mono}^{SMAP}), is designed to jointly retrieve SM and VOD with high accuracy while minimizing reliance on auxiliary optical constraints (Li et al., 2022a). Evaluation has shown that the IB_{mono}^{SMAP} SM dataset performs comparably or favorably against other SMAP products under varying environmental conditions (Yi et al., 2023; Fan et al., 2023). Its VOD product also shows less saturation and stronger correlations with independent forest structure indicators (*e.g.,* tree height, biomass) than optical-constrained VOD datasets (Li et al., 2022a; Peng et al., 2024).

Launched in late 2009, the SMOS mission was the first satellite specifically designed for L-band radiometry and has delivered continuous global observations since 2010. Through its large Y-shaped antenna, the SMOS mission measures dual-polarized and multi-angle TB across the land surface, with incidence angles spanning from 2.5° to 62.5°. This rich observational capability enables the simultaneous retrieval of SM and VOD via the L-MEB (L-band Microwave Emission of the Biosphere) model (Wigneron et al., 2007; Al Bitar et al., 2017; Wigneron et al., 2017). Currently, three primary physically-based retrieval datasets retrieved from SMOS TBs are widely used, including the Level 2 product (Kerr et al., 2012), the Level 3 product (Al Bitar et al., 2017), and SMOS-IC (hereafter referred to as IC_{multi}^{SMOS}) (Fernandez-Moran et al., 2017a). Among them, IC_{multi}^{SMOS} represents the most recent algorithm designed to make efficient use of SMOS's multi-angular TB observations. Compared to L2 and L3, IC_{multi}^{SMOS} adopts a simpler algorithmic framework and assumes pixels to be homogeneous in their land surface conditions, thereby reducing reliance on external ancillary datasets to characterize sub-pixel heterogeneity (Li et al., 2020). Additionally, IC_{multi}^{SMOS} also includes optimized parameterizations for key radiative transfer variables including vegetation scattering albedo and soil roughness as detailed in (Wigneron et al., 2021; Liu et 2025; Konkathi et al., 2025). These improvements have contributed to its comparable advantages in multiple comparative analyses (Al-Yaari et al., 2019; Colliander et al., 2023; Ma et al., 2019).

For both the SMOS and SMAP, the quality of the TBs is critical for the accuracy of land parameter retrievals (Kerr et al., 2016; Martin-Neira et al., 2016). SMAP, although a mono-angular instrument, is based on an advanced technology dedicated to filtering Radio-Frequency Interference (RFI) using a 40° incidence angle real-aperture radiometer (Entekhabi et al., 2010). Conversely, SMOS is based on a two-dimensional interferometric radiometer that acquires multi-angular observations but remains very sensitive to RFI effects (Wigneron et al., 2021; Oliva et al., 2016; Peng et al., 2023). Moreover, the incidence angles of SMOS vary with the distance from the swath center, ranging from 0°–55° near the center to about 40°–50° at the swath edges (Rodriguez-Fernandez et al., 2015). At the swath edges, reconstruction noise and aliasing become more pronounced, particularly at low incidence angles within the "extended alias-free" region where sky-alias correction is applied (Martín-Neira et al., 2016). In addition, SMOS exhibits significant daily variations in its angular coverage. Aggregating multi-angular TBs into fixed 5° bins, a method used in the SMOS L3 product, can introduce considerable noise, a limitation noted in prior research (Schmitt and Kaleschke, 2018). Given these limitations, it remains unclear whether improved performance could be obtained by using improved mono-angular SMOS data rather than noisy multi-angular SMOS L3 TB data. This question is very difficult to address presently as all the SMOS products currently available differ in their retrieval algorithms, but they share one common feature: they all use multi-angular SMOS L3 TB measurements to retrieve SM and VOD, rather than using mono-angle TBs similar to SMAP's 40° incidence angle. Developing a mono-angular SMOS product is therefore of practical importance, as it would provide a consistent alternative to the current multi-angular products and enable more coherent cross-mission analyses with SMAP, particularly considering SMOS has far exceeded its initial design life.

In this context, this study aims to develop a mono-angular SMOS product focused on the simultaneous SM and VOD retrievals within the SMAP-IB algorithm framework. In parallel, we also attempted to address the following scientific questions: i) Are SMOS retrievals based solely on 40° TB inherently less accurate than those based on multi-angle TB data? and ii) Under a common algorithmic framework, how does the choice of TB inputs dictate the retrieval accuracy of both SM and VOD? To address these two main questions, we: 1) directly applied the SMAP-IB algorithm to SMOS L3 40° TB to retrieve $IB_{mono}^{RawSMOS}$; 2) applied a fitting procedure to reduce noise in L3 40° TB (hereafter SMOS-IB TB), and then used it to generate IB_{mono}^{SMOSIB}; 3) incorporated a refined soil roughness (Hr) scheme into SMAP-IB to obtain $IB\_HR_{mono}^{SMOSIB}$; 4) evaluated all resulting SM and VOD products against IC_{multi}^{SMOS} and IB_{mono}^{SMAP}, using International Soil Moisture Network (ISMN) (2016–2022) and four vegetation proxies. Comparative analyses revealed that both, the TB optimization procedure and the refined Hr scheme significantly improved the retrieval performance of SM and VOD, making it comparable to SMAP. These improvements led to the development of a 25-km mono-angular SMOS-IB product suite, including optimized TB, SM, and VOD layers (*i.e.,* $IB\_HR_{mono}^{SMOSIB}$), spanning a 15-year period from 2010 to 2024. This is also the first study to generate global SM and VOD datasets simultaneously using only fitted 40° SMOS TB observations. Furthermore, the long-term optimized SMOS-IB 40° TB dataset holds potential for broader applications, such as freeze–thaw monitoring and snow depth estimation.

2 Data and preprocessing

2.1 SMOS Level 3 TB product

We used the SMOS Level-3 (SMOS-L3) TB product distributed by the Centre Aval de Traitement des Données (CATDS) for the years 2010–2024. SMOS-L3 TB provides multi-angle H- and V-polarized TBs recorded at the top of the atmosphere (Al Bitar et al., 2017). Despite the absence of atmospheric correction, the average atmospheric effect remains relatively mild globally, with ~1 K (H-polarization) and ~0.5 K (V- polarization) at 40° (De Lannoy et al., 2015). It should be noted that the SMOS L3 daily multi-angle TB data are obtained using a fixed 5° width binning method, with bin centers lie within the 2.5° - 62.5° interval. Previous studies have revealed that this approach may result in stronger short-term TB fluctuations at specific angles compared to alternative methods, such as two-step regression fitting. This ultimately increases the uncertainty in analyses or retrievals dependent on single-angle TB data (Peng et al., 2023; Schmitt and Kaleschke, 2018; Li et al., 2022b). This work employed the SMOS-L3 TB dataset (on a 25 km EASE-Grid 2.0), utilizing solely the ascending orbit (06:00 am local time) TBs.

2.2 ISMN *in-situ* SM dataset

The ISMN *in-situ* SM measurements (https://ismn.geo.tuwien.ac.at/, accessed on 2025.10.01) were used to evaluate the TB and satellite SM retrievals' accuracy. ISMN was considered to be the most reliable SM dataset and has been extensively utilized as a benchmark in satellite-based SM calibration and validation studies (Dorigo et al., 2021). Here, SM measurements from the 0-5 cm soil depth from 2016 to 2022 incorporating both sparse and dense *in-situ* networks were collected. Note that there is inherent scale mismatch between pixel-derived SM estimates and ground-based SM observation, particularly in the sparse observed networks. To maintain good data quality and minimize the issue of the spatial scale differences, only ISMN *in-situ* SM observations flagged as "Good" were spatially aggregated by averaging all available station observations within each respective 25 km EASE-Grid 2 cell. Ultimately, a total of 464 cells from 23 networks at a EASE-Grid 2.0 25 km scale were retained (Figure. 1 and Table S1).

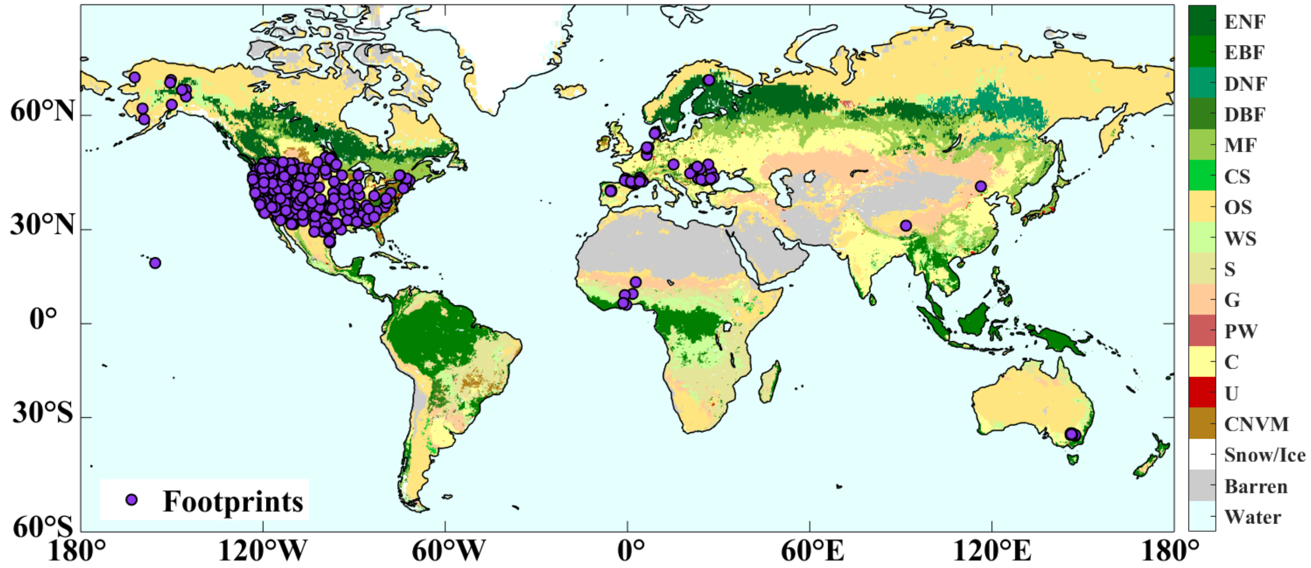

Figure 1: Distribution of the SMOS footprints used for evaluation. The MODIS IGBP land cover map was aggregated to the 25 km grid using the dominant land cover class, resulting in 17 categories: EBF (Evergreen Broadleaf Forest), ENF (Evergreen Needleleaf Forest), DNF (Deciduous Needleleaf Forest), MF (Mixed Forests), DBF (Deciduous Broadleaf Forest), OS (Open Shrublands), WS (Woody Savannas), CS (Closed Shrublands), S (Savannas), G (Grasslands), PM (Permanent Wetland), Water, CNVM (Cropland/Natural vegetation mosaics), C (Croplands), U (Urban), Snow/Ice and Barren. The locations of the ISMN *in-situ* sites are presented in purple dots.

2.3 Vegetation proxies for assessing VOD

Given that the validation of VOD products at large scales is hindered by the lack of a well-established reference dataset, three frequently used vegetation proxies were selected assess the performance of the VOD retrievals (Wigneron et al., 2024), including the 1 km spatial resolution Saatchi aboveground biomass (AGB) map (Saatchi et al., 2011), 0.5° canopy height derived from Global Ecosystem Dynamics Investigation Level 1B LIDAR observations collected between April to July 2019 (Simard et al., 2011), and 1 km resolution 16-day MODIS NDVI data from 2016 to 2022 (Didan, 2021). The canopy height serves as an indicator of total vegetation biomass, and NDVI reflects the greenness and photosynthetic activity within the upper layer canopy (Li et al., 2021). To preserve high-quality observations, the pixels for MODIS NDVI data flagged as 'good quality' were kept following the method of (Grant et al., 2016).

In addition, this study pioneers to use the satellite canopy water content (CWC) data from 2016 to 2022 to validate the temporal behavior of VOD retrievals, since L-band VOD has been demonstrated a linearly relationship with vegetation water content (Wigneron et al., 2020). The CWC product was newly developed by integrating data from Sentinel-2, Landsat-8, and MODIS satellites to monitor canopy vegetation water variations, which has been demonstrated to have good accuracy and reliability, thus providing a robust reference for assessing VOD data (Ma et al., 2025). The dataset is currently distributed through personal communication but will soon be publicly available via ESA data portal. These four vegetation parameters were standardized through projection onto the EASE-Grid 2.0 and spatially aggregated to 25 km using arithmetic mean resampling to match the SMOS grid spatial resolution. This same resampling method has also been employed in several earlier VOD studies (Li et al., 2021; Fan et al., 2019).

2.4 Additional microwave TB, SM, and VOD products used for inter-comparison

To evaluate the performance of optimized SMOS-IB TB (see method Section 3.1) and the $IB\_HR_{mono}^{SMOSIB}$, IB_{mono}^{SMOSIB}, $IB_{mono}^{RawSMOS}$ SM and VOD retrievals, two other L-band TB data (*i.e.,* SMOS-L3 TB and SMAP-L3 TB) and two other L-band satellite global SM and VOD datasets (*i.e.,*IC_{multi}^{SMOS} and IB_{mono}^{SMAP}) were collected.

The SMOS-L3 TB product has been detailed in section 2.1. SMAP-L3 TBs were sourced from the Version 5 SMAP enhanced L3 radiometer SM product collected during the morning (06:00 am local time) descending overpass for the period 2016-2022 (Chan et al., 2018). The SMAP-L3 TB observations were quality controlled based on corresponding quality flags and resampled to 25 km via weighted area averaging for consistency with the SMOS' grid resolution (Li et al., 2022b).

The IC_{multi}^{SMOS} and IB_{mono}^{SMAP} SM and VOD products at 25 km projected onto the EASE-Grid 2.0 from 2016 to 2022 were collected. (1) The IC_{multi}^{SMOS} corresponds to the SMOS-IC dataset, originally developed by (Fernandez-Moran et al., 2017a; Fernandez-Moran et al., 2017b), and is among the most recent SMOS products available. It was retrieved using the processed multi-angle SMOS-L3 TB dataset with quality filtering provided by the CATDS using the SMOS-IC version 2 algorithm. The 25 km SMOS-IC V2 SM and VOD data retrieved from the morning ascending orbit was utilized; (2) The IB_{mono}^{SMAP} was retrieved by applying the SMAP-IB algorithm to the 25km SMAP-L3 TBs (resampled from the 9 km SMAP-L3 TB dataset) at 40° incidence angle (Li et al., 2022a). Readers refer to (Wigneron et al., 2021) and (Li et al., 2022a) for detailed information about the SMOS-IC and SMAP-IB algorithm.

All datasets were evaluated specifically at the 6:00 am local overpass time to capitalize on optimal surface thermal equilibrium conditions characteristic of early morning periods (Entekhabi et al., 2010), following rigorous quality-controlled preprocessing that adhered to each product's specific flagging criteria. For example, the IC_{multi}^{SMOS} and IB_{mono}^{SMAP} unreliable retrievals were effectively removed based on two quality control thresholds: "Scene Flags" > 1 and "TB-RMSE" > 8 K (Wigneron et al., 2021).

Table 1: Summary of the three TB products and five SM and VOD products used and generated in this study.

Category	Product name	Sensor	Incidence angle	Algorithm	Metadata period	Sampling	Reference
TB	SMOS-IB	SMOS	40°	-	2010-2024	Daily, 25 km	Generated in this study
	SMOS-L3	SMOS	40°	-	2010-2024	Daily, 25 km	(Al Bitar et al., 2017)
	SMAP-L3	SMAP	40°	-	2010-2024	Daily, 9 km	(Chan et al., 2018)
SM and VOD	$IB\_HR_{mono}^{SMOSIB}$	SMOS	40°	SMAP-IB	2010-2024	Daily, 25 km	Generated in this study
	IB_{mono}^{SMOSIB}	SMOS	40°	SMAP-IB	2010-2024	Daily, 25 km	Generated in this study
	$IB_{mono}^{RawSMOS}$	SMOS	40°	SMAP-IB	2010-2024	Daily, 25 km	Generated in this study
	IC_{multi}^{SMOS}	SMOS	20°-55°	SMOS-IC	2010-2024	Daily, 25 km	(Wigneron et al., 2021)
	IB_{mono}^{SMAP}	SMAP	40°	SMAP-IB	2015-2022	Daily, 36 km	(Li et al., 2022a)

2.5 Ancillary datasets

The MODIS IGBP land cover classification (Friedl and Sulla-Menashe, 2022) was employed to analyze SM comparison results across different land cover types. Daily precipitation data at a resolution of 0.1°, sourced from the ERA5-Land reanalysis dataset, was collected and applied to analyze seasonal variation of the SM and VOD datasets (Muñoz-Sabater et al., 2021).

To obtain robust evaluation results, we additionally employed Triple Collocation Analysis (TCA), which provides an independent error estimate and is not affected by the representativeness errors originating from the spatial discrepancy between site points and satellite footprints (see Section 3.1.3). For this purpose, the active microwave Advanced Scatterometer (ASCAT) surface SM product and the model-based Global Land Data Assimilation System (GLDAS-Noah) SM product from 2016 to 2022 were obtained (Rodell et al., 2004). (1) ASCAT, onboard the Meteorological Operation-A, -B and -C satellite, acquires C-band V-polarized backscatter measurements on both ascending and descending orbits (Wagner et al., 2006). The ASCAT SM product is generated from MetOp satellite backscatter measurements using a TU Wien algorithm (Wagner et al., 2013). The ASCAT CDR(Climate Data Record) v7-H119 SM dataset at 12.5 km resolution was used, with its relative SM values converted to volumetric units (m^3/m^3) based on soil porosity from the Harmonized World Soil Database (HWSD). (2) The GLDAS-Noah SM product, with 3-hourly temporal and 0.25° spatial resolution, is derived from the Noah Land Surface Model within the Global Land Data Assimilation System (Rodell et al., 2004). The GLDAS SM (kg/m^2) was also transformed into volumetric unit (m^3/m^3), with daily average SM computed for analysis (Xing et al., 2021). Both the ASCAT and GLDAS-Noah SM were aggregated to 25 km resolution by applying the arithmetic mean resampling to match the SMOS grid resolution.

3 Methods

Figure 2 illustrates the methodological framework, encompassing three major components: SMOS-L3 multi-angle TB optimization, SM and VOD inversion, and performance evaluation.

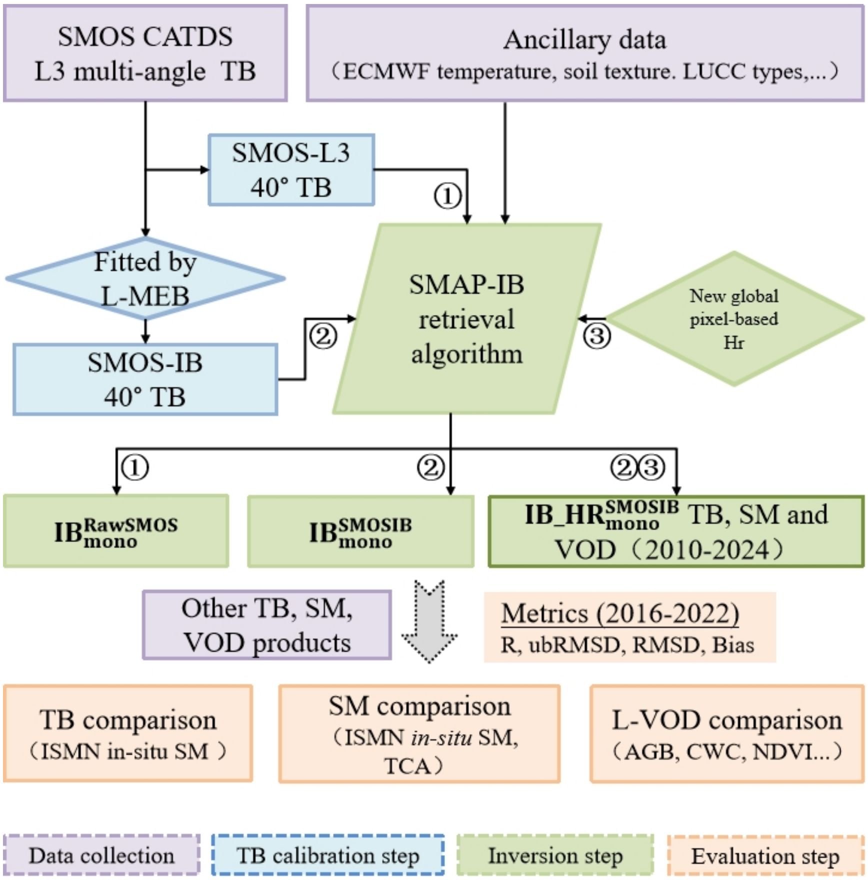

Figure 2: Flow chart illustrating the workflow from data production and performance assessment of ①$IB^{RawSMOS}_{mono}$, ②IB^{SMOSIB}_{mono} and ③$IB_HR^{SMOSIB}_{mono}$: inputs (purple), SMOS-IB TB calibration (blue), SM and VOD inversion (green) and performance assessment (orange).

3.1 Generation of SMOS-IB TB through optimization of SMOS-L3 multi-angle TB

To mitigate the angular-related noise and enhance the consistency of TBs, we adopted the L-MEB model, originally developed for the SMOS and shown to effectively reproduce SMOS TBs across varies land surface conditions (Wigneron et al., 2012). In our implementation, L-MEB was employed as a forward model, with multi-angular SMOS L3 TB as input. The optimal fitting results were obtained by minimizing the RMSE (root mean square error) between the L-MEB simulated and observed TB values. Figure 3 shows examples of the fitting results on May 5, June 15, July 3, and August 8, 2024. It can be seen that the fitted TBs significantly reduce the irregularity and dispersion present in the raw L3 TBs, for both polarizations. The fitted TBs at 40° incidence angle, which is in line with SMAP observations, were used as the SMOS-IB product for subsequent applications. In addition, the fitted TB-RMSE for each pixel was retained in the dataset, as it has been shown to serve as a simple and effective indicator for assessing the real influence of RFI on SMOS TBs' quality (Li et al., 2022; Wigneron et al., 2021).

https://doi.org/10.5194/essd-2025-728
Preprint. Discussion started: 26 January 2026

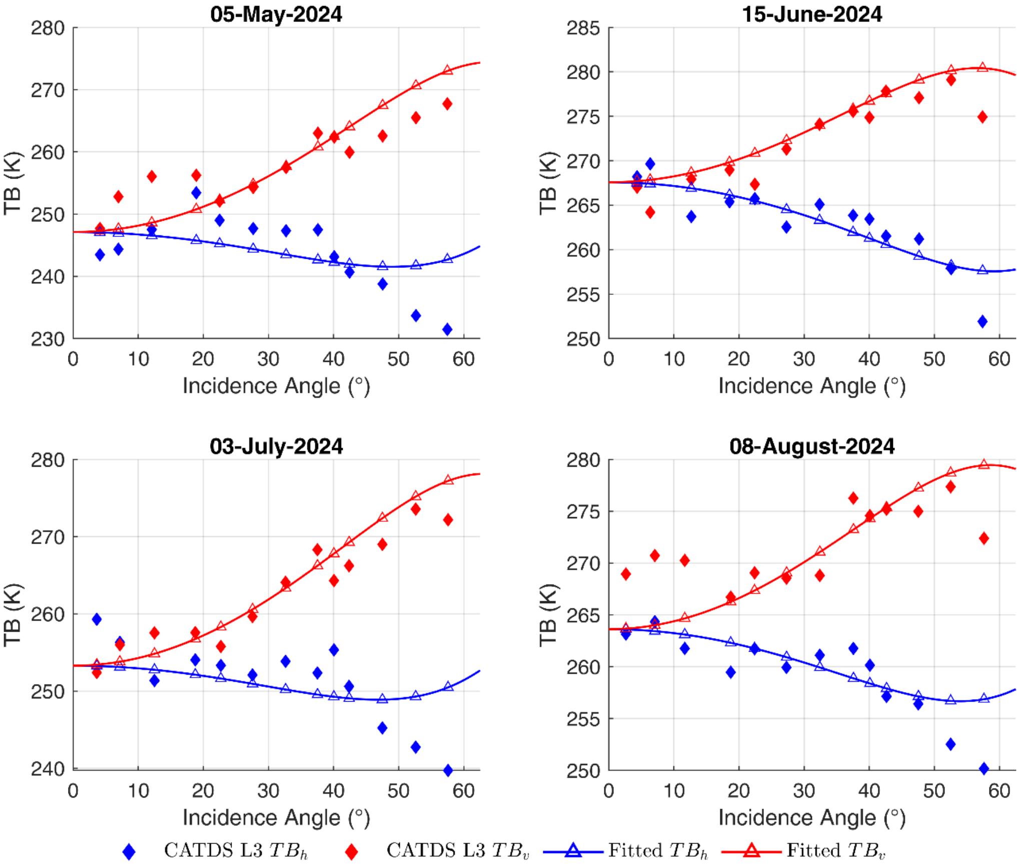

Figure 3: Examples of L-MEB model fitting to CATDS L3 TB at a SMOS pixel located at 83.646°E, 31.661°N. Panels (a) – (d) correspond to May 5, June 15, July 3, and August 8, 2024, respectively.

3.2 SM and VOD inversion using SMAP-IB algorithm

Note that three types of SM and VOD datasets were produced with the aim to address the key scientific questions of this study: ①$IB_{mono}^{RawSMOS}$: implementing the SMAP-IB to the raw SMOS-L3 40° TB; ②IB_{mono}^{SMOSIB}: implementing the SMAP-IB to the SMOS-IB 40° TB, and ③$IB_HR_{mono}^{SMOSIB}$: implementing the SMAP-IB algorithm that incorporated a refined soil roughness (Hr) parameterization scheme to the SMOS-IB 40° TB.

The Tau-Omega (τ-ω) radiative transfer approach was used to compute microwave TB from land surfaces (Mo et al., 1982), which includes three parts: (1) direct upwelling soil emission attenuated by the canopy $T_G(1-r_{G_P})\gamma_P$; (2) direct upwelling canopy emission $T_C(1-\omega)(1-\gamma_P)$; and (3) downwelling canopy emission reflected upward by the soil $T_C(1-\gamma_P)\gamma_{G_P}\gamma_P$:

$$TB_P = T_G(1-r_{G_P})\gamma_P + T_C(1-\omega)(1-\gamma_P) + T_C(1-\gamma_P)r_{G_P}\gamma_P \qquad (1)$$

https://doi.org/10.5194/essd-2025-728
Preprint. Discussion started: 26 January 2026

where T_C and T_G are the effective temperatures of vegetation and soil (*K*), computed using ERA5 soil and skin temperatures; γ_P denotes the vegetation attenuation factor, estimated as $\gamma_P = exp(-VOD/cos\theta)$; The effective scattering albedo ω was assigned according to the IGBP land cover types (Kurum, 2013). r_{G_P} represents the soil reflectivity and is computed using the H-Q-N semi-empirical model developed by (Wang and Choudhury, 1981), which combines the smooth-surface reflectivity (r_{GP}^*) with a roughness correction governed by Hr. In this study, we used the values of a novel global calibrated pixel-level Hr data (Konkathi et al., 2025). Their approach moves beyond prior methods, which only accounted for *HR* differences between vegetation types, by also incorporating intra-type *HR* differences through a methodology that synergistically combines radiative transfer modeling with machine learning.

The $IB\_HR_{mono}^{SMOSIB}$ SM and VOD were jointly retrieved based on the optimized SMOS 40° incidence angle TBs using SMAP-IB algorithm, incorporating the values of a novel global calibrated Hr. To resolve the underdetermined problem of 2-Parameter retrieval from correlated SMOS TB observations, the SMAP-IB method implements an optimized least-squares iteration, which minimizes a cost function (*CF*) that accounts for prior knowledge of SM and VOD.

$$CF = \frac{\sum(TB_p^{mes} - TB_p^*)^2}{\sigma(TB)^2} + \frac{\sum(SM^{ini} - SM^*)^2}{\sigma(SM)^2} + \frac{\sum(VOD^{ini} - VOD^*)^2}{\sigma(VOD)^2} \tag{2}$$

where TB_p^{mes} (TB_p^*) denote the measured and simulated TBs at both polarizations, respectively; $\sigma(\cdot)$ is the standard deviation operator; and the second and third terms are regularization functions that involve the retrieval parameters (SM^*, VOD^*) and their initial estimates (SM^{ini}, VOD^{ini}). Please refer to (Li et al., 2022a) for a detail description of these initial estimations of the SMAP-IB algorithm.

3.3 Evaluation of TB, SM and VOD

Four key metrics were applied to examine the performance of the retrieved dataset: (1) Pearson's correlation coefficient (*R*; Eq. 3), (5) systematic bias (Eq. 4), (3) RMSD (Eq. 5), and (4) unbiased RMSD (*ub*RMSD; Eq. 6) (Entekhabi et al., 2010).

$$R = \sqrt{1 - \frac{(\theta_{RS} - \theta_{REF})^2}{(\theta_{RS} - \overline{\theta_{REF}})^2}} \tag{3}$$

$$Bias = \underline{\theta_{RS} - \theta_{REF}} \tag{4}$$

$$RMSD = \sqrt{\overline{(\theta_{RS} - \theta_{REF})^2}} \tag{5}$$

$$ubRMSD = \sqrt{RMSD^2 - Bias^2} \tag{6}$$

where θ_{RS} is the satellite TB, SM or VOD dataset; θ_{REF} is the reference data; the overbar represents the temporal averaging operator (*i.e.*, $\overline{\theta_{REF}}$). Since systematic biases between observations and satellite retrievals may distort RMSD, the *ub*RMSD and *R* typically provide more reliable metrics for validation (Xing et al., 2021).

3.3.1 TB and SM evaluation

(1) *In-situ* based metrics

The retrieved SM data were rigorously validated against the ISMN *in-situ* observations. Concurrently, the sensitivity of TB to *in-situ* SM was quantitatively evaluated. This analysis is based on the well-established physical principle of a negative TB-SM correlation: as SM increases, the consequent rise in the soil's dielectric constant reduces its microwave emissivity, leading to a decrease in observed TB. Following the method of early studies (Yi et al., 2023; Xing et al., 2023), a three-step analysis was applied to retain valid evaluation result to ensure fair comparisons: (1) all datasets were assessed for the consistent period from 2016 to 2022, (2) maximum 1-hour temporal matching between *in-situ* data and satellite overpasses, (3) minimum 31 valid observations (*i.e.,* 1 month) per station for statistical robustness, and (4) restriction to the same stations containing valid evaluation metrics for all TB or SM datasets. TB assessment focused on *R* to evaluate radiometric consistency, while SM evaluation employed four metrics (*R*, bias, RMSD, and *ub*RMSD). Note that we also performed paired t-tests to quantify whether the differences in each of the two TB or SM products' performance metrics are statistically significant (null hypothesis: equal means between product pairs; α=0.05).

(2) TCA-based metrics

The direct validation of the SM retrievals using sparse *in-situ* networks may not be sufficient for obtaining a robust evaluation result due to potential representativeness errors associated with the spatial discrepancy between obseved SM and satellite SM observations (Al-Yaari et al., 2019; Xing et al., 2021). The TCA method was employed as a secondary evaluation approach for SM quality evaluation, owing to its applicability at the footprint as well as pixel scale (Dong and Crow, 2017). Before conducting TCA, we preprocessed the SM data by removing the climatological seasonal signal from each product to avoid potential overestimation in TCA metrics that could arise from inter-product climatology correlations (Dong et al., 2020; Kim et al., 2020). The SM anomalies were computed as below:

$$\theta_{anom}(t) = \theta_t - \overline{\theta_{(t-17:t+17)}} \tag{7}$$

where $\theta_{anom}(t)$ is the SM anomalies at day *t* and $\overline{\theta_{(t-17:t+17)}}$ is the mean SM value via a 35-day moving window (Fan et al., 2022a).

Given that the TCA method requires strictly independent error structures across its three collocated SM products, we adopted the conventional triplet configuration proposed by Gruber et al. (2020), including passive (*i.e.,* $IB\_HR_{mono}^{SMOSIB}$, IB_{mono}^{SMOSIB}, $IB_{mono}^{RawSMOS}$, IC_{multi}^{SMOS} and IB_{mono}^{SMAP}), active microwave product (*i.e.,* ASCAT) and a model-based SM product (*i.e.,* GLDAS-Noah). The analysis specifically examined the TCA-derived correlation coefficient (hereafter referred to as TCA-*R*) as the primary metric of product performance. Please refer to (Fan et al., 2022a) and (Dong and Crow, 2017) for more information about the TCA method.

3.3.2 VOD evaluation

The performance of VOD was assessed using two complementary approaches: (1) spatial *R* (VOD vs. AGB/canopy height) and (2) temporal *R* (VOD *vs.* CWC) and *R* (VOD *vs.* NDVI), following previous studies (Chaparro et al., 2019; Zotta et al., 2024; Li et al., 2021). Daily VOD were composited into 16-day intervals in order to align with the NDVI data, while retaining only statistically significant *R* with a p-value < 0.05.

3.4 The $IB\_HR_{mono}^{SMOSIB}$ dataset

The global $IB\_HR_{mono}^{SMOSIB}$ dataset is archived in netCDF4 format and mapped to EASE-Grid 2.0, featuring a 584 × 1388 grid with a 25 km sampling resolution. The dataset contains 14 layers (Table 2), including TB, SM, and VOD, their associated uncertainty layers, expressed as the standard errors of SM and VOD, and the global soil roughness map. The RMSE values layer between the measured and modeled TB and the Scene_Flags layer are also included in the dataset. The RMSE layer, the optimal fitting results obtained by minimizing the RMSE between the L-MEB simulated and observed TB values, serves as a measure of RFI influence on the TBs and to filter out SM and VOD data substantially influenced by RFI. The Scene_Flags layer is used to filter out multiple impacts linked to specific climate or topographic conditions (Table 2). The datasets for the period 2010-2024 can be freely downloaded at website (https://zenodo.org/records/17647385) (Xing et al., 2025) and will be continuously maintained on the INRAE Bordeaux Remote Sensing Product website (https://ib.remote-sensing.inrae.fr/).

Table 2: Overview of the gridded data layers included in the $IB\_HR_{mono}^{SMOSIB}$ dataset.

Data layer	Description	Units
CRS	Coordinate reference systems (CRS) include spatial reference information and geographic transformation parameters	/
lat	The latitude of the center of each grid cell	degree
lon	The longitude of the center of each grid cell	degree
Incidence_Angle	Pixel-based Incidence Angle	degree
TIME_UTC	Year information starting from 2010	/
BT_H	Optimized brightness temperature at H polarization	K
BT_V	Optimized brightness temperature at V polarization	K
Soil_Moisture	Soil Moisture (SM) retrievals	m^3/m^3
Soil_Moisture_StdError	Error on the derived Soil Moisture	m^3/m^3
Optical_Thickness_Nad	Vegetation Optical Depth (VOD) retrievals	/
Optical_Thickness_Nad_StdError	Error on the derived Vegetation Optical Depth	/
Soil_Roughness	Global Soil Roughness Map	/
RMSE	Goodness-of-fit between measured TB and modelled TB (Root Mean Square Error, RMSE)	K
Scene_Flags	8-bit flag '00000001': moderate Topography '00000010': strong Topography '00000100': polluted scene (water+urban+ice > 10% of the pixel), '00001000': frozen scene, ECMWF_Surf_Temperature < 273K	/

https://doi.org/10.5194/essd-2025-728
Preprint. Discussion started: 26 January 2026

4 Result and discussions

4.1 Evaluation of the optimized TB

The global spatial pattern of high-frequency TB variations was quantified by calculating the standard deviation (SDHF) of TB after removing seasonal cycle for SMOS-IB, SMAP-L3, and SMOS-L3 (Figure 3). It was observed that the high-frequency variability was consistently higher in H-polarization than in V-polarization across all products, particularly in water-limited regions. Critically, the spatial median SDHF for both SMOS-IB and SMAP-L3 was low and comparable (< 5.33 K), whereas SMOS-L3 exhibited markedly higher variability (> 7.20 K). This demonstrated that SMOS-IB and SMAP-L3 shared similarly low noise levels, while SMOS-L3 retained the strongest high-frequency fluctuations. These differences reflected their distinct processing chains: unlike the top of atmosphere SMOS-L3 TB, SMAP-L3 included atmospheric correction and dedicated RFI mitigation, and SMOS-IB benefited from noise reduction via L-MEB model optimization, bringing its variability characteristics closer to those of SMAP-L3. Spatially, SMOS-L3 showed markedly higher SDHF than the other two products over central and northeastern Africa, central and eastern Asia, and parts of eastern Europe, regions that coincide with known RFI hotspots for SMOS (Wigneron et al., 2021; Al-Yaari et al., 2019). Pixel-wise SDHF differences further reinforced these patterns (Figure S1): deviations between SMOS-IB and SMAP-L3 were minimal (within ±0.02 over most regions), whereas SMOS-L3 showed systematically higher values, particularly over the above-mentioned RFI-affected areas where differences relative to both SMOS-IB and SMAP-L3 typically exceeded 5 K. These results confirmed that SMOS-L3 preserved substantial high-frequency noise, while SMOS-IB and SMAP-L3 provided cleaner temporal TB profiles (Figure S2).

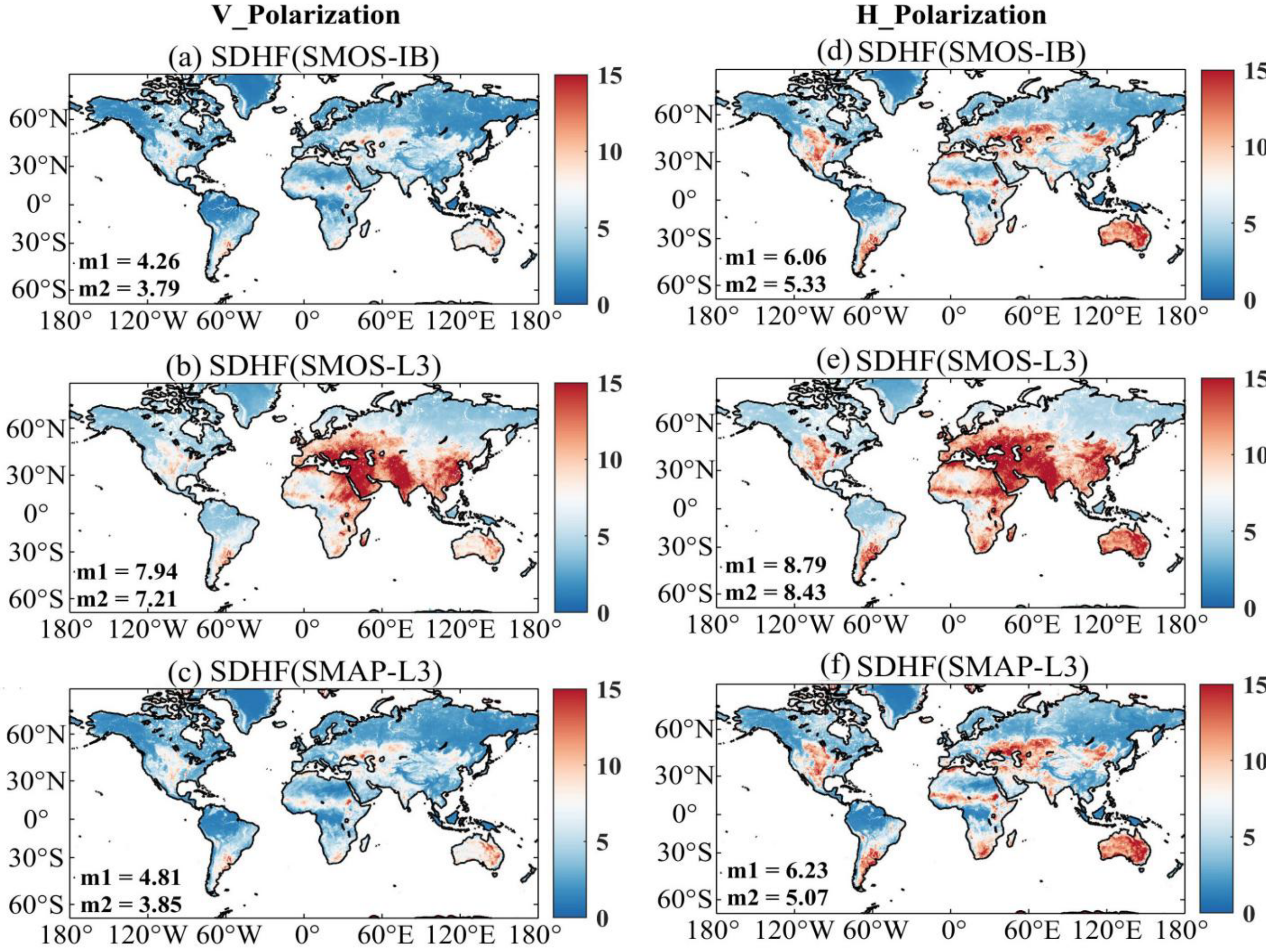

Figure 4 Maps of the standard deviation of the high-frequency variations (SDHF) in the TB time series for (a) SMOS-IB, (b) SMOS-L3 and (c) SMAP-L3 TB in V-polarization, and (d) - (f) in H-polarization. SDHF was derived by removing the seasonal cycle, which was computed with a 30-day moving window average filter. m1 and m2 denote the spatial mean and median SDHF value (unit: k), respectively.

To further investigate how the three TB products respond to SM variations, we assessed their sensitivity to ISMN in-situ SM using the coefficient of determination (R^2) across 12 MODIS IGBP land cover types (Table 3). Overall, all three products showed the strongest SM sensitivity in shrublands (S), with R^2 values exceeding 0.80 for both polarizations, and the weakest sensitivity in barren or sparsely vegetated areas, where R^2 values fell below 0.30, reflecting the reduced radiometric sensitivity of microwave observations in regions with low SM dynamics. The land cover-specific analysis confirmed and extended the overall patterns described above: SMAP-L3 TB generally presented the highest R^2 values, followed closely by SMOS-IB TB, while SMOS-L3 TB showed the lowest sensitivity to ISMN *in-situ* SM data. This ranking pattern (SMAP-L3 > SMOS-IB >

SMOS-L3 TB) showed complete consistency across all land cover types for H-polarization and in 7 of 12 cases for V-polarization, respectively. Particularly, SMOS-IB TB achieved slightly higher R^2 than SMAP-L3 TB in MF, CS, OS, WS, S and G land cover types. These findings indicated that the proposed optimization process effectively enhanced the sensitivity of SMOS TB to SM and enabled SMOS-IB to achieve performance levels comparable to SMAP-L3 TB in most cases.

Table 3 Coefficient of determination (R^2) between ISMN *in-situ* measurements and the satellite-based TB products (SMOS-IB, SMOS-L3, and SMAP-L3) for both polarizations during 2016–2022, used to assess the sensitivity of TB to SM across the 12 MODIS IGBP land cover types. Red < yellow < green indicates the color coding from the lowest to highest R² values, and, for each product, the land cover type with the highest TB–SM R² is highlighted in bold.

Polarization	Product	ENF	EBF	DBF	MF	CS	OS	WS	S	G	C	CNVM	Barren	Overall
H-polarization	SMOS-IB	0.40	0.46	0.39	0.43	0.58	0.43	0.50	**0.87**	0.53	0.50	0.65	0.22	0.48
	SMOS-L3	0.33	0.41	0.33	0.29	0.53	0.40	0.42	**0.85**	0.50	0.48	0.57	0.19	0.45
	SMAP-L3	0.41	0.54	0.40	0.43	0.58	0.45	0.51	**0.87**	0.54	0.51	0.69	0.23	0.49
V-polarization	SMOS-IB	0.41	0.41	0.36	0.42	0.59	0.45	0.50	**0.90**	0.57	0.49	0.67	0.19	0.49
	SMOS-L3	0.36	0.18	0.35	0.32	0.57	0.40	0.45	**0.85**	0.53	0.47	0.61	0.17	0.44
	SMAP-L3	0.41	0.48	0.40	0.40	0.57	0.44	0.49	**0.89**	0.56	0.49	0.70	0.22	0.49

4.2 Evaluation of the SM retrievals

4.2.1 ISMN *in-situ* SM-based comparison

Figure 5 presents the overall evaluation performance of $IB\_HR_{mono}^{SMOSIB}$ SM against ISMN *in-situ* measurements, indicated by median values of R, *ub*RMSD, RMSD, and Bias, with comparative analysis of four other SM products (IB_{mono}^{SMOSIB}, $IB_{mono}^{RawSMOS}$, IC_{multi}^{SMOS} and IB_{mono}^{SMAP}) from 2016 to 2022. Regarding R and *ub*RMSD, $IB\_HR_{mono}^{SMOS}$ SM achieved similarly high performance with IB_{mono}^{SMOSIB} and IB_{mono}^{SMAP}, with all three products reaching a median R of 0.67 and a median *ub*RMSD of ~0.059 m³/m³. In comparison, IC_{multi}^{SMOS} and $IB_{mono}^{RawSMOS}$yielded lower median R of 0.65 and 0.64, respectively, and higher *ub*RMSD of 0.063 m³/m³ (Figure 5(a)-(b)). Particularly, the better performance of $IB_HR_{mono}^{SMOSIB}$and IB_{mono}^{SMOSIB}SM products over $IB_{mono}^{RawSMOS}$ SM demonstrated that high-quality TB data enabled more accurate SM retrievals. This was further supported by the time series comparison in Figure S3, which showed that the $IB_{mono}^{RawSMOS}$ SM product exhibited higher noise levels in its retrievals—a direct consequence of the noisier TB input. Since these products employed the same inversion method (*i.e.,* SMAP-IB algorithm) but differed in SMOS TB inputs, the results underscored the critical role of pre-processed TB quality in enhancing SM estimation accuracy from the data side (leaving algorithm improvements aside). Besides, the $IB\_HR_{mono}^{SMOSIB}$, IB_{mono}^{SMOSIB} and IB_{mono}^{SMAP} performed better than the IC_{multi}^{SMOS} SM product, indicating that, when supported by a sufficiently robust retrieval algorithm, a mono-angular approach was not necessarily inferior to a multi-angular one. Regarding RMSD, the $IB\_HR_{mono}^{SMOSIB}$, IB_{mono}^{SMOSIB}, IC_{multi}^{SMOS}, and IB_{mono}^{SMAP} SM products (RMSD ranged from 0.093 to 0.097 m³/m³) exhibited marginally lower errors compared to $IB_{mono}^{RawSMOS}$ (RMSD = 0.100 m³/m³) (Fig. 5(c)). All five SM datasets were dryer than observed SM, as illustrated by a negative bias (satellite SM minus *in-situ* SM), in which IC_{multi}^{SMOS} (Bias = -0.058 m³/m³) had a lower bias compared to the

https://doi.org/10.5194/essd-2025-728
Preprint. Discussion started: 26 January 2026

other four SM products (Bias ranges from -0.067 to -0.061 m³/m³) (Fig. 5(d)). These findings were in agreement with the evaluation results indicted in Li et al. (2022b).

To systematically assess the accuracy of the $IB\_HR_{mono}^{SMOSIB}$ SM dataest across diverse networks, we computed *in-situ* network-level median statistics for three statistical metrics including *R*, *ub*RMSD, and Bias (Table S2). In terms of *ub*RMSD, $IB\_HR_{mono}^{SMOSIB}$ achieved the lowest error in 10 out of 23 networks, followed closely by IB_{mono}^{SMAP} with 9 out of 23, and they outperformed IC_{multi}^{SMOS} and $IB_{mono}^{RawSMOS}$ in both the number of networks and their overall *ub*RMSD levels. Regarding *R*, IB_{mono}^{SMAP} acquired the highest accuracy over the other four SM products in 52% of the networks, followed by IB_{mono}^{SMOSIB} and $IB\_HR_{mono}^{SMOSIB}$. Across networks, all five satellite SM products showed their strongest agreement with observation in the AMMA-CATCH network, where they achieved uniformly high *R* values (≥ 0.88) and low error metrics (*ub*RMSD ≤ 0.03 m³/m³), meeting the typical L-band mission accuracy requirement of ~0.04 m³/m³. In contrast, the FMI network *in-situ* SM recorded the lowest *R* values (≤ 0.51), and the SNOTEL network *in-situ* SM showed the highest *ub*RMSD values (≥ 0.075 m³/m³) for all products. However, the retrieval performance in these networks was not uniformly degraded across all metrics; for example, the FMI network still exhibited reasonable *ub*RMSD levels, while the SNOTEL network retained moderate *R* values. These patterns indicated that the limitations arose from different aspects of the retrieval, suggesting room for further improvement in these regions. IC_{multi}^{SMOS} acquired the lowest Bias of the five SM products over 11 observation networks, though all SM products exhibited similar median dry biases (-0.056 to -0.067 m³/m³).

https://doi.org/10.5194/essd-2025-728
Preprint. Discussion started: 26 January 2026

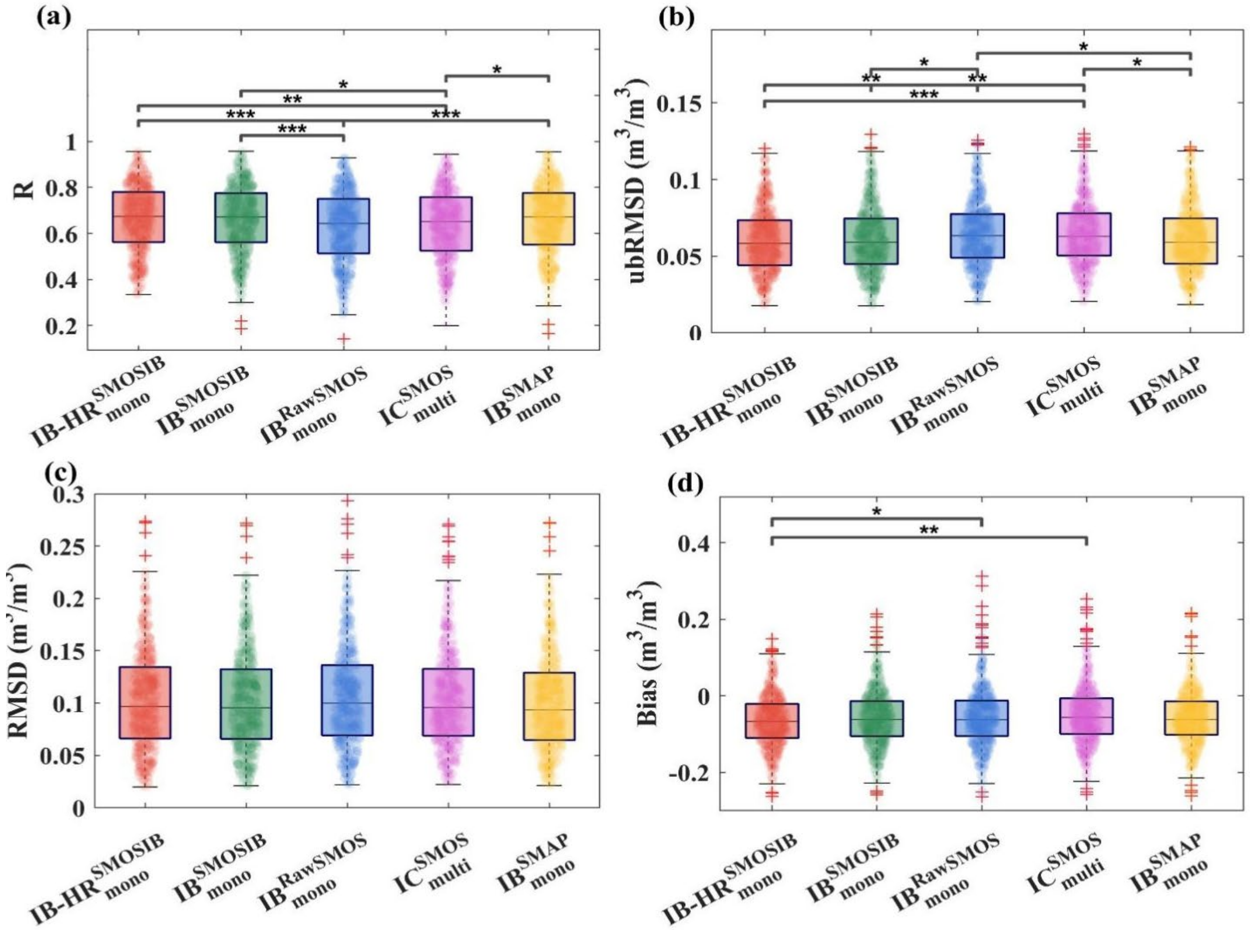

Figure 5: Boxplots summarizing the overall metrics of $IB\_HR_{mono}^{SMOSIB}$, IB_{mono}^{SMOSIB}, $IB_{mono}^{RawSMOS}$, IC_{multi}^{SMOS}, and IB_{mono}^{SMAP} against ISMN *in-situ* SM regarding (a) *R*, (b) *ub*RMSD (m^3/m^3), (c) RMSD (m^3/m^3) and (d) Bias (m^3/m^3) from 2016 to 2022. The scatter points in the boxplot represent individual data points. The symbols *, **, and * indicate that the *P-Value* computed from the two-sample t-test between the metrics of each two products is below 0.05, 0.01, and 0.001, respectively.**

https://doi.org/10.5194/essd-2025-728
Preprint. Discussion started: 26 January 2026

Figure 6 shows the site-level scatterplots of *ΔR* (difference in *R*) and *Δub*RMSD (difference in *ub*RMSD) between each pair of SM products for the ISMN *in-situ* sites covered by non-forest and forest LUCC types. The purpose was to assess whether improvements in correlation and *ub*RMSD occured simultaneously at the site scale. Based on the number of sites showing concurrent gains in both metrics, $IB\_HR_{mono}^{SMOSIB}$ consistently outperformed $IB_{mono}^{RawSMOS}$ and IC_{multi}^{SMOS} SM across both forest and non-forest regions, as evidenced by pairwise metric differences: $IB\_HR_{mono}^{SMOSIB}$ showed positive *ΔR* (higher correlation) and negative *Δub*RMSD over 84% and 78% of non-forest *in-situ* sites, respectively. This advantage also persisted in forest regions with positive *ΔR* and negative *Δub*RMSD over 84% and 53% of the *in-situ* sites (Figure. 6(a), (b), (a1) and (b1)). These results demonstrated the robust performance of $IB\_HR_{mono}^{SMOSIB}$ across diverse land cover types, reconfirming the advancements achieved by the advanced TB observations ($IB\_HR_{mono}^{SMOSIB}$ *vs.* $IB_{mono}^{RawSMOS}$) and mono-angel angular algorithm ($IB\_HR_{mono}^{SMOSIB}$ *vs.* IC_{multi}^{SMOS}). Notably, compared with $IB_{mono}^{RawSMOS}$, $IB\_HR_{mono}^{SMOSIB}$ achieved absolute *ub*RMSD reductions greater than 0.01 m^3/m^3 and *R* increased above 0.10 at several forest and non-forest sites, further confirming the effectiveness of the optimized TB fitting. Besides, a better performance of $IB\_HR_{mono}^{SMOSIB}$ than IB_{mono}^{SMOSIB} (in 31.83% and 41.75% of the *in-situ* sites) and IB_{mono}^{SMAP} (in 48% and 43% of the *in-situ* sites) was also observed across both non-forest and forest regions (Figure. 6(c), (d), (c1) and (d1)). This improvement underscored the benefit of the new Hr parameterization scheme, which further enhanced SM retrieval accuracy beyond what was achievable with optimized TB data alone. In addition, both IC_{multi}^{SMOS} and $IB_{mono}^{RawSMOS}$ demonstrated lower accuracy than IB_{mono}^{SMAP} over 74% and 79% of the non-forest sites and 56% and 74% of the forest sites (Figure 6(e), (f), (e1) and (f1)). These findings also confirmed that algorithmic refinements—particularly in TB calibration and in the optimization of key radiative transfer parameters—can bridge the performance gap between SMOS and SMAP, making $IB\_HR_{mono}^{SMOSIB}$ a reliable high-precision product for hydrological and climate applications. These results aligned with the finding of (Colliander et al., 2023) and (Colliander et al., 2022), who found that both SMOS and SMAP L-band radiometers exhibited comparable sensitivity to SM variations.

https://doi.org/10.5194/essd-2025-728
Preprint. Discussion started: 26 January 2026

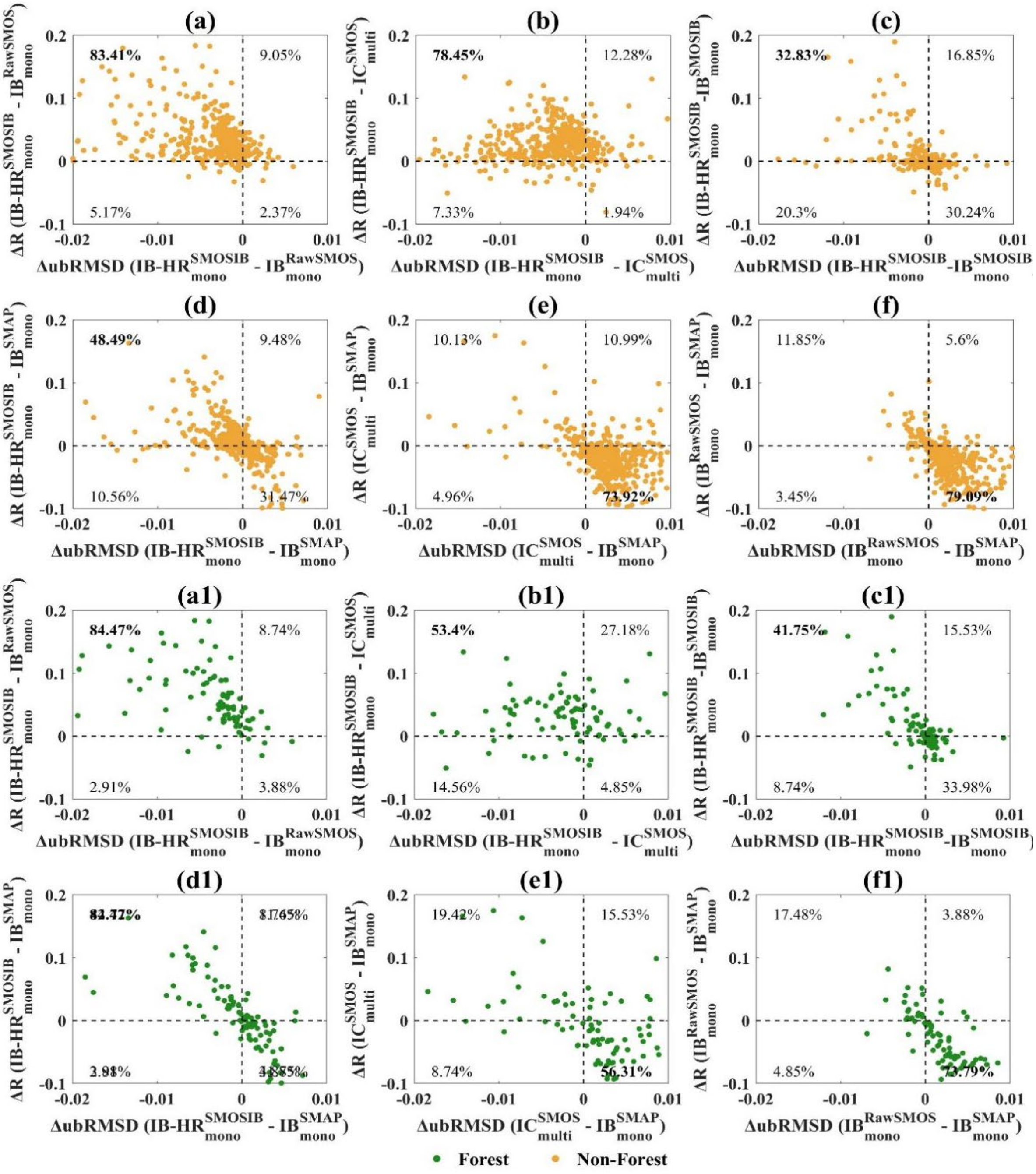

Figure 6: Scatterplots of Δ*R* (difference in correlation coefficient) and Δ*ub*RMSD (difference in unbiased RMSD) between paired soil moisture datasets for the ISMN *in-situ* sites. The colors of the symbols represent the (a-f) non-forest (orange) and (a1-f1) forest (green), aggregated based on MODIS IGBP LUCC types.

4.2.2 TCA-based comparison

We then used TCA-R to evaluate the pixel-scale performance of SM anomaly estimates from five satellite products (Figure 7 and Figure S4). Overall, the IB_{mono}^{SMAP} SM product performed the best with higher TCA-R values across most regions (spatial median TCA-R = 0.81), followed by $IB\_HR_{mono}^{SMOS\mathrm{IB}}$, IB_{mono}^{SMOSIB} and IC_{multi}^{SMOS} with spatial median TCA-R ranging from 0.75 to 0.76 (Figure S4(a)-(d)). In contrast, $IB_{mono}^{RawSMOS}$displayed lower accuracy, with a spatial median TCA-R of only 0.58, indicating a notable performance gap compared to the other four SM products (Figure S4(c)). Similar to the ISMN *in-situ* measurements-based evaluation result, the performance ranking for the five SM products was maintained, suggesting robust consistency between the two independent SM evaluation approaches. The spatial patterns and histograms of the TCA-R differences between paired SM products showed absolute median spatial differences in TCA-R of 0.001 and 0.150 (Figure 7). Notably, the aligned evaluation results indicated that these performance differences for the five SM products originate from TB inputs and the inherent differences in SM retrieval algorithms. $IB\_HR_{mono}^{SMOSIB}$ demonstrated a clear and consistent performance advantage over most other SM products, including $IB_{mono}^{RawSMOS}$, IC_{multi}^{SMOS} and IB_{mono}^{SMOSIB}, as illustrated in Figures 7(a) - (c) and 7(f) - (h).

The performance gap between $IB_HR_{mono}^{SMOSIB}$and $IB_{mono}^{RawSMOS}$ was particularly striking, evidenced by both an overwhelmingly red global map, which indicated widespread positive ΔR values, and high median ΔR of 0.107 (Figures 7(a) and (f)). This pronounced visual and quantitative contrast reconfirmed our finding that robust TBs is fundamental to obtaining more accurate SM retrievals. Regarding the performance difference of $IB\_HR_{mono}^{SMOSIB}$ *vs.* IC_{multi}^{SMOS} and IB_{mono}^{SMOSIB}, the differences in TCA-R values were distributed with a centroid near zero (absolute mean ΔR = 0.005, median ΔR < 0.002), indicating generally consistent performance between these three SM products across most regions, while the extended tails of these distributions reveal non-negligible discrepancies in certain areas (Figure 7(g) and (h)). It is noteworthy that IB_{mono}^{SMOSIB} exhibited a distinct deficiency in the northern high latitudes compared to $IB\_HR_{mono}^{SMOSIB}$. This resulted from the improved parameterization of surface roughness in the Northern Hemisphere in the new Hr scheme. Unlike the original Hr scheme, which prescribed generally low roughness values solely based on land cover type, the new Hr scheme used in $IB_HR_{mono}^{SMOSIB}$more accurately captured the characteristically high per-pixel roughness there (Figure S5). This improvement was primarily attributed to the scheme's ability to incorporate the significant influence of high soil organic carbon in the northern high latitude regions (Konkathi et al., 2025).

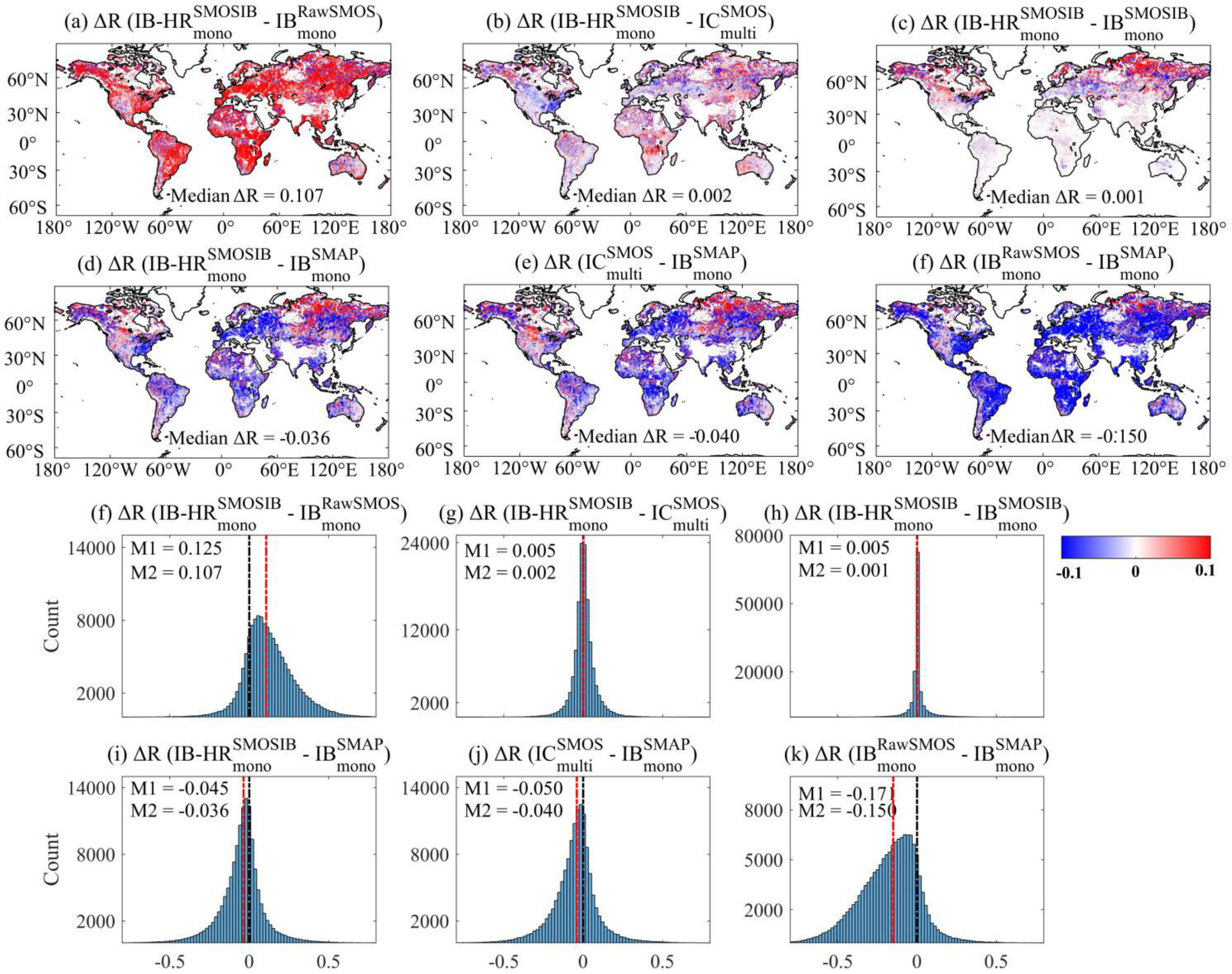

Figure 7: Spatial distribution ((a)–(e)) and histograms ((f)–(k)) of TCA-based R differences between paired SM anomaly products. m1 and m2 denote the mean and median (red line) difference value. A black vertical line marks the zero-difference reference.

4.3 Evaluation of the VOD retrievals

Figure 8 presents the spatial density distributions of the five VOD datasets against the aboveground biomass (AGB) map. It was found that the four VOD products showed very similar R values, ranging only from 0.84 for IC^{SMOS}_{multi} and 0.85 for $IB\_HR^{SMOSIB}_{mono}$, IB^{SMOSIB}_{mono} and IB^{SMAP}_{mono}, whereas $IB^{RawSMOS}_{mono}$ had the lowest R values of 0.80. Moreover, all five VOD products effectively captured the spatial gradients of AGB, yielding the same highest R values of 0.87 when comparing predicted and observed AGB (Figure 8(a) - (e)). Similarly, the $IB\_HR^{SMOSIB}_{mono}$, IB^{SMOSIB}_{mono} and IB^{SMAP}_{mono} VOD products exhibited the same highest spatial R value (0.90) when correlated with forest canopy height, indicating a strong linear relationship–even for tall trees. Followed by $IB\_HR^{SMOSIB}_{mono}$ and $IB^{RawSMOS}_{mono}$ with spatial R of 0.89 and 0.87 (Figure S6). This aligned with previous VOD validation studies (Zotta et al., 2024; Li et al., 2021; Rodríguez-Fernández et al., 2018), as L-band VOD responded to the full vertical structure of vegetation, encompassing woody components (Frappart et al., 2020). These findings suggested that, in terms of spatial patterns, it was difficult to distinguish clear advantages among the five products. Nevertheless, given the comparable influence of VOD and Hr in the τ–ω model and their strong coupling (Eq.1), we plotted each VOD product against the corresponding Hr used in its retrieval (Figure 8(a1) - (e1)). It was found that $IB\_HR^{SMOSIB}_{mono}$ VOD demonstrated a notably weaker spatial correlation with its Hr ($R = 0.39$) than the other VOD products using IGBP-based Hr schemes ($R > 0.70$). This decoupling effect was particularly evident in forested areas, where the spatial R between $IB\_HR^{SMOSIB}_{mono}$ VOD and Hr (R = -0.36) was the lowest among all products, while the others showed R > 0.57. These findings collectively indicate that the new Hr scheme effectively mitigated the coupling effect with VOD, leading to more physically independent VOD retrievals compared with the IGBP-based Hr schemes.

The per-pixel temporal correlation coefficient between the five VOD datasets and CWC were also calculated to examine the discrepancy of the temporal performances for the VOD datasets (Figure 9). All VOD products exhibited consistent spatial patterns in their temporal R values with vegetation dynamics, particularly across eastern US, southern Africa, eastern Brazil, Siberia, and Australia (Figure. 9a–d), with the $IB^{RawSMOS}_{mono}$VOD product showing particularly widespread non-significant pixels across these biomes (Figure. 9e). Figure 9(f) identifies the VOD dataset with the strongest per-pixel temporal R values (absolute R difference > 0.1) after excluding non-significant pixels. It was found that IB^{SMAP}_{mono}, $IB\_HR^{SMOSIB}_{mono}$ and IB^{SMOS}_{multi} demonstrated highest R values with CWC across 41 %, 24 % and 21 % of the analyzed pixels, respectively, with these pixels mainly located in mid- to low-latitude regions (*e.g.,* Australia, South, East and West Africa, and America). Similar findings were also obtained when NDVI was used as a reference (Figure S7). It is noteworthy that the temporal R between $IB_HR^{SMOSIB}_{mono}$and CWC was generally higher than that derived using IB^{SMOSIB}_{mono} across most regions globally, particularly in high vegetated regions (*e.g.,* Australia, Central North America, Amazon, Central Africa, *etc.*). This finding underscored the advantage of incorporating optimized Hr inputs in VOD retrievals, because the key distinction between the two VOD products lied in the optimization of roughness inputs. Similarly, Konkathi et al. (2025) also showed that the improved VOD-NDVI correlation in these regions resulted from their refined Hr scheme, which mitigated SM and VOD compensations (Figure S8).

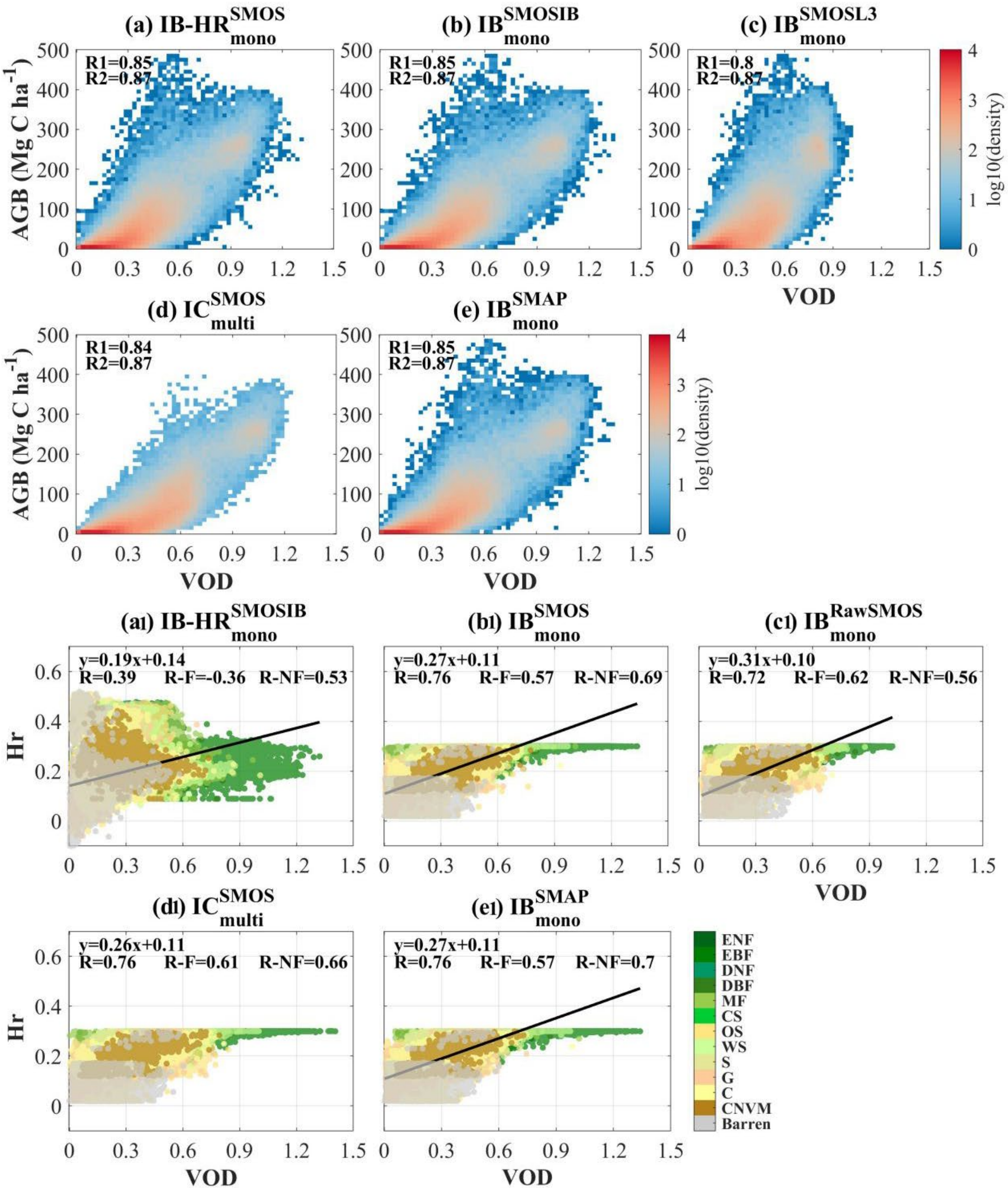

Figure 8: Global density plots of VOD *vs.* AGB for five products: (a)$IB\_HR^{SMOSIB}_{mono}$, (b) IB^{SMOSIB}_{mono}, (c) $IB^{RawSMOS}_{mono}$, (d) IC^{SMOS}_{multi} and (e) IB^{SMAP}_{mono}. R1 denotes the correlation coefficient between VOD and AGB, and R2 denotes the R between VOD-predicted AGB and reference AGB. Panels (a1–e1) show VOD *vs.* Hr scatter plots for the same products, with spatial correlations reported for all pixels (R), forest pixels (R-F) and non-forest pixels (R-NF).

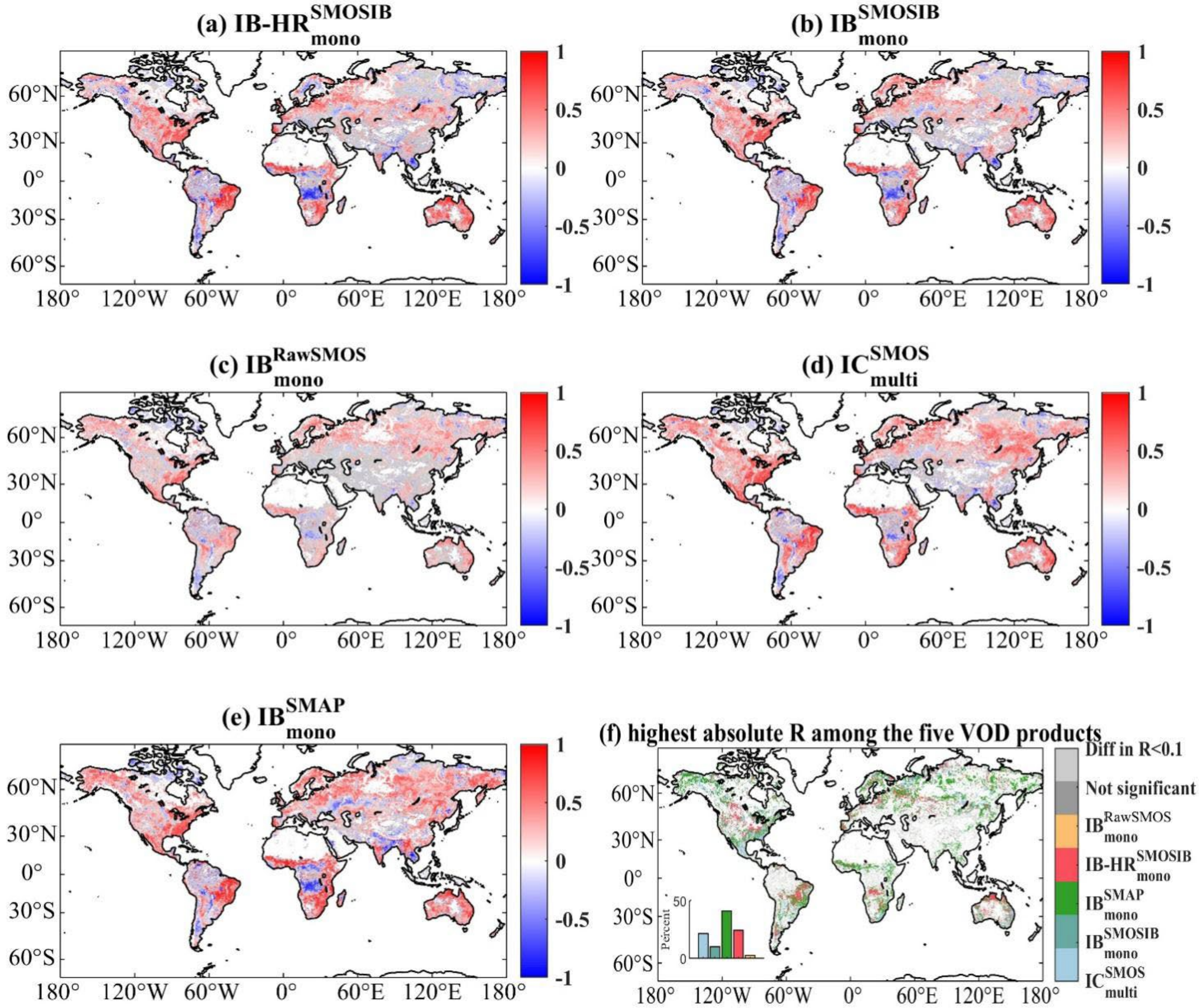

Figure 9: Temporal correlation between VOD and CWC (2016–2022) for (a) $IB\_HR^{SMOSIB}_{mono}$, (b) IB^{SMOSIB}_{mono}, (c) $IB^{RawSMOS}_{mono}$, (d) IC^{SMOS}_{multi} and (e) IB^{SMAP}_{mono}. (f) maps of the above five VOD products with the highest absolute R values with CWC. Non-significant R are represented by dark grey pixels ($p > 0.05$), and the light grey color indicates pixels with R difference for each paired VOD product < 0.1. White areas represent "no valid data".

5 Data availability

The global SMOS-IB TB, SM and VOD datasets for the period 2010-2024 can be freely downloaded at (https://zenodo.org/records/17647385) (Xing et al., 2025) and will be continuously maintained on the INRAE Bordeaux Remote Sensing Product website (https://ib.remote-sensing.inrae.fr/).

6 Conclusion and outlook

In this study, we first generated an optimized global 40° SMOS TB dataset and then derived the corresponding mono-angular SM and VOD datasets using the SMAP-IB retrieval framework. This mono-angular approach was specifically designed to isolate and investigate the underlying causes of performance differences between existing SMOS and SMAP products retrieved from different algorithms and satellite observations. To achieve this, a comprehensive evaluation of $IB\_HR_{mono}^{SMOSIB}$ TB, SM and VOD retrievals was conducted against ISMN *in-situ* SM data and four vegetation parameters (*i.e.,* CWC, Saatchi AGB, canopy height, and MODIS NDVI), by inter-comparison with other four datasets (*i.e.,* IB_{mono}^{SMOSIB}, $IB_{mono}^{RawSMOS}$, IC_{multi}^{SMOS}, and IB_{mono}^{SMAP}). The following key conclusions are drawn:

(1) Our evaluation showed that the newly developed $IB\_HR_{mono}^{SMOSIB}$ dataset demonstrated robust performance for TB as well as SM and VOD retrievals. Specifically, the optimized 40° SMOS-IB TB had markedly lower noise than the SMOS-L3 TB and provided global accuracy comparable to SMAP-L3. Correspondingly, the $IB\_HR_{mono}^{SMOSIB}$ SM product derived from SMOS-IB TB also achieved an accuracy (median R of 0.67, *ub*RMSD of 0.059 m³/m³) comparable to IB_{mono}^{SMAP}. Moreover, it clearly outperformed IC_{multi}^{SMOS} (median R of 0.65, *ub*RMSD of 0.063 m³/m³) and $IB_{mono}^{RawSMOS}$(median R of 0.64, *ub*RMSD of 0.063 m³/m³).

(2) Regarding VOD retrievals, although all five products exhibited similar spatial relationships with AGB (R ~ 0.85), the new Hr scheme effectively decoupled surface roughness from vegetation contributions, thereby enabling more physically-based $IB\_HR_{mono}^{SMOSIB}$ VOD retrievals. Consistently, the temporal correlation between $IB\_HR_{mono}^{SMOSIB}$ and CWC was generally higher than that obtained using IB_{mono}^{SMOSIB} in moderate to high vegetated regions, further confirming the role of optimized Hr inputs in the $IB\_HR_{mono}^{SMOSIB}$ VOD retrievals.

(3) Under the same algorithmic framework, the better performance of $IB\_HR_{mono}^{SMOSIB}$ and IB_{mono}^{SMOSIB} SM products over $IB_{mono}^{RawSMOS}$ SM demonstrated that high-quality TB inputs enabled more accurate SM retrievals. Building on this, the refined Hr retrieval scheme further improved performance, as $IB\_HR_{mono}^{SMOSIB}$ performed better than IB_{mono}^{SMOSIB} in many *in-situ* networks, with particularly enhanced accuracy in the northern high latitudes. Our results demonstrated that a mono-angular approach was not necessarily less effective than a multi-angular one. In particular, the combined use of optimized mono-angular observations and an advanced retrieval algorithm (e.g., SMAP-IB) can yield better results than multi-angle approaches (e.g., the SMOS-IC algorithm).

Our evaluation demonstrated that the mono-angular SMOS-IB TB, SM and VOD products achieved performance comparable to SMAP product, while outperforming multi-angular SMOS products in most cases. Therefore, SMOS-IB holds potential for broader applications, such as drought monitoring, assessing vegetation water dynamics for plant stress evaluation, and supporting eco-hydrological studies. This study also contributed to the longstanding issue about the relative importance of algorithm design versus instrument characteristics in L-band radiometry. Our findings provided evidence that future mission development should prioritize both the refinement and selection of suitable retrieval algorithms and improvements in TB observation quality. Taken together, these results offered valuable scientific insights for guiding future algorithm selection and supporting the continued advancement of upcoming satellite missions.

Author Contributions

XJL and JPW conceived the study. ZPX conducted the analyses and prepared the manuscript. XZL contributed to data preprocessing, and HLM provided the CWC dataset. All authors contributed to methodological discussions and offered feedback on both the manuscript and the data.

Declaration of Competing Interest

The authors declare that they have no known competing financial interests or personal relationships that could have appeared to influence the work reported in this manuscript. All the authors listed have approved the manuscript that is enclosed.

Acknowledgements

This research has been supported by the Foundation for Innovative Research Groups of the National Natural Science Foundation of China (Grant No. 42421001), and the National Natural Science Foundation of China (Grant No. 42501480).

References

Al-Yaari, A., Wigneron, J. P., Dorigo, W., Colliander, A., Pellarin, T., Hahn, S., Mialon, A., Richaume, P., Fernandez-Moran, R., Fan, L., Kerr, Y. H., and De Lannoy, G.: Assessment and inter-comparison of recently developed/reprocessed microwave satellite soil moisture products using ISMN ground-based measurements, Remote Sensing of Environment, 224, 289-303, 10.1016/j.rse.2019.02.008, 2019.

Al Bitar, A., Mialon, A., Kerr, Y. H., Cabot, F., Richaume, P., Jacquette, E., Quesney, A., Mahmoodi, A., Tarot, S., Parrens, M., Al-Yaari, A., Pellarin, T., Rodriguez-Fernandez, N., and Wigneron, J.-P.: The global SMOS Level 3 daily soil moisture and brightness temperature maps, Earth System Science Data, 9, 293-315, 10.5194/essd-9-293-2017, 2017.

Baur, M. J., Friend, A. D., and Pellegrini, A. F. A.: Widespread and systematic effects of fire on plant–soil water relations, Nature Geoscience, 17, 1115-1120, 10.1038/s41561-024-01563-6, 2024.

Chaparro, D., Duveiller, G., Piles, M., Cescatti, A., Vall-llossera, M., Camps, A., and Entekhabi, D.: Sensitivity of L-band vegetation optical depth to carbon stocks in tropical forests: a comparison to higher frequencies and optical indices, Remote Sensing of Environment, 232, 10.1016/j.rse.2019.111303, 2019.

De Lannoy, G. J. M., Reichle, R. H., Peng, J., Kerr, Y., Castro, R., Kim, E. J., and Qing, L.: Converting Between SMOS and SMAP Level-1 Brightness Temperature Observations Over Nonfrozen Land, IEEE Geoscience and Remote Sensing Letters, 12, 1908-1912, 10.1109/lgrs.2015.2437612, 2015.

Chan, S. K., Bindlish, R., O'Neill, P., Jackson, T., Njoku, E., Dunbar, S., Chaubell, J., Piepmeier, J., Yueh, S., Entekhabi, D., Colliander, A., Chen, F., Cosh, M. H., Caldwel, T., Walker, J., Berg, A., McNairn, H., Thibeault, M., Martinez-Fernandez, J., Uldall, F., Seyfried, M., Bosch, D., Starks, P., Collins, C. H., Prueger, J., van der Velde, R., Asanuma, J., Palecki, M., Small, E. E., Zreda, M., Calvet, J. C., Crow, W. T., and Kerr, Y.: Development and Assessment of the SMAP Enhanced Passive Soil Moisture Product, Remote Sens Environ, 204, 931-941, 10.1016/j.rse.2017.08.025, 2018.

Chan, S. K., Bindlish, R., O'Neill, P. E., Njoku, E., Jackson, T., Colliander, A., Chen, F., Burgin, M., Dunbar, S., Piepmeier, J., Yueh, S., Entekhabi, D., Cosh, M. H., Caldwell, T., Walker, J., Wu, X., Berg, A., Rowlandson, T., Pacheco, A., McNairn, H., Thibeault, M., Martinez-Fernandez, J., Gonzalez-Zamora, A., Seyfried, M., Bosch, D., Starks, P., Goodrich, D., Prueger, J., Palecki, M., Small, E. E., Zreda, M., Calvet, J.-C., Crow, W. T., and Kerr, Y.: Assessment of the SMAP Passive Soil Moisture Product, IEEE Transactions on Geoscience and Remote Sensing, 54, 4994-5007, 10.1109/tgrs.2016.2561938, 2016.

Colliander, A., Kerr, Y., Wigneron, J. P., Al-Yaari, A., Rodriguez-Fernandez, N., Li, X., Chaubell, J., Richaume, P., Mialon, A., Asanuma, J., Berg, A., Bosch, D. D., Caldwell, T., Cosh, M. H., Holifield Collins, C., Martínez-Fernández, J., McNairn, H., Seyfried, M. S., Starks, P. J., Su, Z., Thibeault, M., and Walker, J. P.: Performance of SMOS Soil Moisture Products over Core Validation Sites, IEEE Geoscience and Remote Sensing Letters, 1-1, 10.1109/lgrs.2023.3272878, 2023.

Colliander, A., Reichle, R. H., Crow, W. T., Cosh, M. H., Chen, F., Chan, S., Das, N. N., Bindlish, R., Chaubell, J., Kim, S., Liu, Q., O'Neill, P. E., Dunbar, R. S., Dang, L. B., Kimball, J. S., Jackson, T. J., Al-Jassar, H. K., Asanuma, J., Bhattacharya, B. K., Berg, A. A., Bosch, D. D., Bourgeau-Chavez, L., Caldwell, T., Calvet, J.-C., Collins, C. H., Jensen, K. H., Livingston, S., Lopez-Baeza, E., Martinez-Fernandez, J., McNairn, H., Moghaddam, M., Montzka, C., Notarnicola, C., Pellarin, T., Greimeister-Pfeil, I., Pulliainen, J., Ramos, J. G., Seyfried, M., Starks, P. J., Su, Z., van der Velde, R., Zeng, Y., Thibeault, M., Vreugdenhil, M., Walker, J. P., Zribi, M., Entekhabi, D., and Yueh, S. H.: Validation of Soil Moisture Data Products From the NASA SMAP Mission, IEEE Journal of Selected Topics in Applied Earth Observations and Remote Sensing, 15, 364-392, 10.1109/jstars.2021.3124743, 2022.

De Lannoy, G. J. M., Reichle, R. H., Peng, J., Kerr, Y., Castro, R., Kim, E. J., and Qing, L.: Converting Between SMOS and SMAP Level-1 Brightness Temperature Observations Over Nonfrozen Land, IEEE Geoscience and Remote Sensing Letters, 12, 1908-1912, 10.1109/lgrs.2015.2437612, 2015.

Didan, K.: MODIS/Terra Vegetation Indices 16-Day L3 Global 500m SIN Grid V061 [Data set]. NASA EOSDIS Land Processes Distributed Active Archive Center, Accessed 2023-08-01 from https://doi.org/10.5067/MODIS/MOD13A1.061, 2021.

Dong, J. and Crow, W. T.: An Improved Triple Collocation Analysis Algorithm for Decomposing Autocorrelated and White Soil Moisture Retrieval Errors, Journal of Geophysical Research: Atmospheres, 122, 13,081-013,094, 10.1002/2017jd027387, 2017.

Dong, J., Crow, W. T., Tobin, K. J., Cosh, M. H., Bosch, D. D., Starks, P. J., Seyfried, M., and Collins, C. H.: Comparison of microwave remote sensing and land surface modeling for surface soil moisture climatology estimation, Remote Sensing of Environment, 242, 10.1016/j.rse.2020.111756, 2020.

Dorigo, W., Himmelbauer, I., Aberer, D., Schremmer, L., Petrakovic, I., Zappa, L., Preimesberger, W., Xaver, A., Annor, F., Ardö, J., Baldocchi, D., Blöschl, G., Bogena, H., Brocca, L., Calvet, J.-C., Camarero, J. J., Capello, G., Choi, M., Cosh, M. C., Demarty, J., van de Giesen, N., Hajdu, I., Jensen, K. H., Kanniah, K. D., de Kat, I., Kirchengast, G., Rai, P. K., Kyrouac, J., Larson, K., Liu, S., Loew, A., Moghaddam, M., Martínez Fernández, J., Mattar Bader, C., Morbidelli, R., Musial, J. P., Osenga, E., Palecki, M. A., Pfeil, I., Powers, J., Ikonen, J., Robock, A., Rüdiger, C., Rummel, U., Strobel, M., Su, Z., Sullivan, R., Tagesson, T., Vreugdenhil, M., Walker, J., Wigneron, J. P., Woods, M., Yang, K., Zhang, X., Zreda, M., Dietrich, S., Gruber, A., van Oevelen, P., Wagner, W., Scipal, K., Drusch, M., and Sabia, R.: The International Soil Moisture Network: serving Earth system science for over a decade, Hydrogeology and Earth System Sciences, 25, 5749–5804, 10.5194/hess-2021-2, 2021.

Entekhabi, D., Njoku, E. G., O'Neill, P. E., Kellogg, K. H., Crow, W. T., Edelstein, W. N., Entin, J. K., Goodman, S. D., Jackson, T. J., Johnson, J., Kimball, J., Piepmeier, J. R., Koster, R. D., Martin, N., McDonald, K. C., Moghaddam, M., Moran, S., Reichle, R., Shi, J. C., Spencer, M. W., Thurman, S. W., Tsang, L., and Van Zyl, J.: The Soil Moisture Active Passive (SMAP) Mission, Proceedings of the IEEE, 98, 704-716, 10.1109/jproc.2010.2043918, 2010.

Fan, L., Xing, Z., Lannoy, G. D., Frappart, F., Peng, J., Zeng, J., Li, X., Yang, K., Zhao, T., Shi, J., Ma, H., Wang, M., Liu, X., Yi, C., Ma, M., Tang, X., Wen, J., Chen, X., Wang, C., Wang, L., Wang, G., and Wigneron, J.-P.: Evaluation of satellite and reanalysis estimates of surface and root-zone soil moisture in croplands of Jiangsu Province, China, Remote Sensing of Environment, 282, 10.1016/j.rse.2022.113283, 2022a.

Fan, L., Wigneron, J.-P., Ciais, P., Chave, J., Brandt, M., Sitch, S., Yue, C., Bastos, A., Li, X., Qin, Y., Yuan, W., Schepaschenko, D., Mukhortova, L., Li, X., Liu, X., Wang, M., Frappart, F., Xiao, X., Chen, J., Ma, M., Wen, J., Chen, X., Yang, H., van Wees, D., and Fensholt, R.: Siberian carbon sink reduced by forest disturbances, Nature Geoscience, 16, 56-62, 10.1038/s41561-022-01087-x, 2022b.

Fan, L., Wigneron, J. P., Ciais, P., Chave, J., Brandt, M., Fensholt, R., Saatchi, S. S., Bastos, A., Al-Yaari, A., Hufkens, K., Qin, Y., Xiao, X., Chen, C., Myneni, R. B., Fernandez-Moran, R., Mialon, A., Rodriguez-Fernandez, N. J., Kerr, Y., Tian, F., and Penuelas, J.: Satellite-observed pantropical carbon dynamics, Nat Plants, 5, 944-951, 10.1038/s41477-019-0478-9, 2019.

Fernandez-Moran, R., Al-Yaari, A., Mialon, A., Mahmoodi, A., Al Bitar, A., De Lannoy, G., Rodriguez-Fernandez, N., Lopez-Baeza, E., Kerr, Y., and Wigneron, J.-P.: SMOS-IC: An Alternative SMOS Soil Moisture and Vegetation Optical Depth Product, Remote Sensing, 9, 10.3390/rs9050457, 2017a.

Fernandez-Moran, R., Wigneron, J. P., De Lannoy, G., Lopez-Baeza, E., Parrens, M., Mialon, A., Mahmoodi, A., Al-Yaari, A., Bircher, S., Al Bitar, A., Richaume, P., and Kerr, Y.: A new calibration of the effective scattering albedo and soil roughness parameters in the SMOS SM retrieval algorithm, International Journal of Applied Earth Observation and Geoinformation, 62, 27-38, 10.1016/j.jag.2017.05.013, 2017b.

Frappart, F., Wigneron, J.-P., Li, X., Liu, X., Al-Yaari, A., Fan, L., Wang, M., Moisy, C., Le Masson, E., Aoulad Lafkih, Z., Vallé, C., Ygorra, B., and Baghdadi, N.: Global Monitoring of the Vegetation Dynamics from the Vegetation Optical Depth (VOD): A Review, Remote Sensing, 12, 10.3390/rs12182915, 2020.

Friedl, M., & Sulla-Menashe, D. (2022). MODIS/Terra+Aqua Land Cover Type Yearly L3 Global 500m SIN Grid V061 [Data set]. NASA Land Processes Distributed Active Archive Center. https://doi.org/10.5067/MODIS/MCD12Q1.061 Date Accessed: 2025-10-23

Gao, L., Sadeghi, M., and Ebtehaj, A.: Microwave retrievals of soil moisture and vegetation optical depth with improved resolution using a combined constrained inversion algorithm: Application for SMAP satellite, Remote Sensing of Environment, 239, 10.1016/j.rse.2020.111662, 2020a.

Gao, L., Sadeghi, M., Feldman, A. F., and Ebtehaj, A.: A Spatially Constrained Multichannel Algorithm for Inversion of a First-Order Microwave Emission Model at L-Band, IEEE Transactions on Geoscience and Remote Sensing, 58, 8134-8146, 10.1109/tgrs.2020.2987490, 2020b.

Gao, L., Ebtehaj, A., Chaubell, M. J., Sadeghi, M., Li, X., and Wigneron, J.-P.: Reappraisal of SMAP inversion algorithms for soil moisture and vegetation optical depth, Remote Sensing of Environment, 264, 10.1016/j.rse.2021.112627, 2021.

Grant, J. P., Wigneron, J. P., De Jeu, R. A. M., Lawrence, H., Mialon, A., Richaume, P., Al Bitar, A., Drusch, M., van Marle, M. J. E., and Kerr, Y.: Comparison of SMOS and AMSR-E vegetation optical depth to four MODIS-based vegetation indices, Remote Sensing of Environment, 172, 87-100, 10.1016/j.rse.2015.10.021, 2016.

Gruber, A., De Lannoy, G., Albergel, C., Al-Yaari, A., Brocca, L., Calvet, J. C., Colliander, A., Cosh, M., Crow, W., Dorigo, W., Draper, C., Hirschi, M., Kerr, Y., Konings, A., Lahoz, W., McColl, K., Montzka, C., Muñoz-Sabater, J., Peng, J., Reichle, R., Richaume, P., Rüdiger, C., Scanlon, T., van der Schalie, R., Wigneron, J. P., and Wagner, W.: Validation practices for satellite soil moisture retrievals: What are (the) errors?, Remote Sensing of Environment, 244, 10.1016/j.rse.2020.111806, 2020.

Jackson, T. J.: Measuring surface soil moisture using passive microwave remote sensing, Hydrological Processes, 7, 139-152, 1993.

Kerr, Y. H., Waldteufel, P., Richaume, P., Wigneron, J. P., Ferrazzoli, P., Mahmoodi, A., Al Bitar, A., Cabot, F., Gruhier, C., Juglea, S. E., Leroux, D., Mialon, A., and Delwart, S.: The SMOS Soil Moisture Retrieval Algorithm, IEEE Transactions on Geoscience and Remote Sensing, 50, 1384-1403, 10.1109/tgrs.2012.2184548, 2012.

Kerr, Y. H., Wigneron, J. P., Al Bitar, A., Mialon, A., and Srivastava, P. K.: Soil Moisture from Space, in: Satellite Soil Moisture Retrieval, 3-27, 10.1016/b978-0-12-803388-3.00001-2, 2016.

Kim, H., Wigneron, J.-P., Kumar, S., Dong, J., Wagner, W., Cosh, M. H., Bosch, D. D., Collins, C. H., Starks, P. J., Seyfried, M., and Lakshmi, V.: Global scale error assessments of soil moisture estimates from microwave-based active and passive satellites and land surface models over forest and mixed irrigated/dryland agriculture regions, Remote Sensing of Environment, 251, 10.1016/j.rse.2020.112052, 2020.

Knowles, K.: EASE-Grid Land Cover Classifications Derived from Boston University MODIS/Terra Land Cover Data, Version 1. [Indicate subset used]. Boulder, Colorado USA. NASA National Snow and Ice Data Center Distributed Active Archive Center. https://doi.org/10.5067/J0CJG7RZW3IJ. [Date Accessed]. 10.5067/J0CJG7RZW3IJ, 2004.

Konings, A. G., Piles, M., Rötzer, K., McColl, K. A., Chan, S. K., and Entekhabi, D.: Vegetation optical depth and scattering albedo retrieval using time series of dual-polarized L-band radiometer observations, Remote Sensing of Environment, 172, 178-189, 10.1016/j.rse.2015.11.009, 2016.

Konkathi, P., Li, X., Fernandez-Moran, R., Liu, X., Xing, Z., Frappart, F., Piles, M., Karthikeyan, L., and Wigneron, J.-P.: A novel calibration of global soil roughness effects for SMOS-IC soil moisture and L-VOD products, Remote Sensing of Environment, 329, 10.1016/j.rse.2025.114946, 2025.

Kurum, M.: Quantifying scattering albedo in microwave emission of vegetated terrain, Remote Sensing of Environment, 129, 66-74, 10.1016/j.rse.2012.10.021, 2013.

Li, X., Al-Yaari, A., Schwank, M., Fan, L., Frappart, F., Swenson, J., and Wigneron, J. P.: Compared performances of SMOS-IC soil moisture and vegetation optical depth retrievals based on Tau-Omega and Two-Stream microwave emission models, Remote Sensing of Environment, 236, 10.1016/j.rse.2019.111502, 2020.

Li, X., Wigneron, J.-P., Frappart, F., Fan, L., Ciais, P., Fensholt, R., Entekhabi, D., Brandt, M., Konings, A. G., Liu, X., Wang, M., Al-Yaari, A., and Moisy, C.: Global-scale assessment and inter-comparison of recently developed/reprocessed microwave satellite vegetation optical depth products, Remote Sensing of Environment, 253, 10.1016/j.rse.2020.112208, 2021.

Li, X., Wigneron, J.-P., Fan, L., Frappart, F., Yueh, S. H., Colliander, A., Ebtehaj, A., Gao, L., Fernandez-Moran, R., Liu, X., Wang, M., Ma, H., Moisy, C., and Ciais, P.: A new SMAP soil moisture and vegetation optical depth product (SMAP-IB): Algorithm, assessment and inter-comparison, Remote Sensing of Environment, 271, 10.1016/j.rse.2022.112921, 2022a.

Li, X., Wigneron, J.-P., Frappart, F., Lannoy, G. D., Fan, L., Zhao, T., Gao, L., Tao, S., Ma, H., Peng, Z., Liu, X., Wang, H., Wang, M., Moisy, C., and Ciais, P.: The first global soil moisture and vegetation optical depth product retrieved from fused SMOS and SMAP L-band observations, Remote Sensing of Environment, 282, 10.1016/j.rse.2022.113272, 2022b.

Li, X., Ciais, P., Fensholt, R., Chave, J., Sitch, S., Canadell, J. G., Brandt, M., Fan, L., Xiao, X., Tao, S., Wang, H., Albergel, C., Yang, H., Frappart, F., Wang, M., Bastos, A., Maisongrande, P., Qin, Y., Xing, Z., Cui, T., Yu, L., He, L., Zheng, Y., Liu, X., Liu, Y., De Truchis, A., and Wigneron, J. P.: Large live biomass carbon losses from droughts in the northern temperate ecosystems during 2016-2022, Nat Commun, 16, 4980, 10.1038/s41467-025-59999-2, 2025.

Ma, H., Zeng, J., Chen, N., Zhang, X., Cosh, M. H., and Wang, W.: Satellite surface soil moisture from SMAP, SMOS, AMSR2 and ESA CCI: A comprehensive assessment using global ground-based observations, Remote Sensing of Environment, 231, 10.1016/j.rse.2019.111215, 2019.

Ma, H., Li, X., Zeng, J., Zhang, X., Dong, J., Chen, N., Fan, L., Sadeghi, M., Frappart, F., Liu, X., Wang, M., Wang, H., Fu, Z., Xing, Z., Ciais, P., and Wigneron, J.-P.: An assessment of L-band surface soil moisture products from SMOS and SMAP in the tropical areas, Remote Sensing of Environment, 284, 10.1016/j.rse.2022.113344, 2023.

Martín-Neira, M., Oliva, R., Corbella, I., Torres, F., Duffo, N., Durán, I., Kainulainen, J., Closa, J., Zurita, A., Cabot, F., Khazaal, A., Anterrieu, E., Barbosa, J., Lopes, G., Tenerelli, J., Díez-García, R., Fauste, J., Martín-Porqueras, F., González-Gambau, V., Turiel, A., Delwart, S., Crapolicchio, R., and Suess, M.: SMOS instrument performance and calibration after six years in orbit, Remote Sensing of Environment, 180, 19-39, 10.1016/j.rse.2016.02.036, 2016.

Mo, T., Choudhury, B., Schmugge, T., Wang, J. R., and Jackson, T.: A model for microwave emission from vegetation-covered fields, Journal of Geophysical Research: Oceans, 87, 11229-11237, 1982.

Muñoz-Sabater, J., Dutra, E., Agustí-Panareda, A., Albergel, C., Arduini, G., Balsamo, G., Boussetta, S., Choulga, M., Harrigan, S., Hersbach, H., Martens, B., Miralles, D. G., Piles, M., Rodríguez-Fernández, N. J., Zsoter, E., Buontempo, C., and Thépaut, J.-N.: ERA5-Land: a state-of-the-art global reanalysis dataset for land applications, Earth System Science Data, 13, 4349-4383, 10.5194/essd-13-4349-2021, 2021.

Oliva, R., Daganzo, E., Richaume, P., Kerr, Y., Cabot, F., Soldo, Y., Anterrieu, E., Reul, N., Gutierrez, A., Barbosa, J., and Lopes, G.: Status of Radio Frequency Interference (RFI) in the 1400–1427 MHz passive band based on six years of SMOS mission, Remote Sensing of Environment, 180, 64-75, 10.1016/j.rse.2016.01.013, 2016.

O'Neill, P. E., Chan, S., Njoku, E., Jackson, T., Bindlish, R., and Chaubell, J.: SMAP L3 Radiometer Global Daily 36 km EASE-Grid Soil Moisture, Version 7, NASA National Snow and Ice Data Center Distributed Active Archive Center [dataset], 10.5067/HH4SZ2PXSP6A, 2020.

O'Neill, P. E., Chan, S., Njoku, E. G., Jackson, T., Bindlish, R., Chaubell, J., and Colliander, A.: SMAP Enhanced L3 Radiometer Global and Polar Grid Daily 9 km EASE-Grid Soil Moisture, Version 5 [Data Set], Boulder, Colorado USA. NASA National Snow and Ice Data Center Distributed Active Archive Center, https://doi.org/10.5067/4DQ54OUIJ9DL. Date Accessed 01-03-2023, 2021.

O'Neill, P., Chan, S., Bindlish, R., Chaubell, M., Colliander, A., Chen, F., Dunbar, S., Jackson, T., Peng, J., Mousavi, M., Cosh, M., Bongiovanni, T., Walker, J., Wu, X., Berg, A., McNairn, H., Thibeault, M., Martínez-Fernández, J., González-Zamora, Á., Lopez-Baeza, E., Jensen, K., Seyfried, M., Bosch, D., Starks, P., Collins, C. H., Prueger, J., Su, Z., Velde, R. v. d., Asanuma, J., Palecki, M., Small, E., Zreda, M., Calvet, J., Crow, W., Kerr, Y., Yueh, S., and Entekhabi, D.: Calibration and Validation for the L2/3_SM_P Version 7 and L2/3_SM_P_E Version 4 Data Products, SMAP Project, JPL D-56297, Jet Propulsion Laboratory, Pasadena, CASoil Moisture Active Passive (SMAP) Project, 2021.

Peng, J., Tanguy, M., Robinson, E. L., Pinnington, E., Evans, J., Ellis, R., Cooper, E., Hannaford, J., Blyth, E., and Dadson, S.: Estimation and evaluation of high-resolution soil moisture from merged model and Earth observation data in the Great Britain, Remote Sensing of Environment, 264, 10.1016/j.rse.2021.112610, 2021.

Peng, Z., Zhao, T., Shi, J., Kerr, Y. H., Rodriguez-Fernandez, N. J., Yao, P., and Che, T.: An RFI-suppressed SMOS L-band multi-angular brightness temperature dataset spanning over a decade (since 2010), Sci Data, 10, 599, 10.1038/s41597-023-02499-z, 2023.

Peng, Z., Zhao, T., Shi, J., Hu, L., Rodríguez-Fernández, N. J., Wigneron, J.-P., Jackson, T. J., Walker, J. P., Cosh, M. H., Yang, K., Lu, H., Bai, Y., Yao, P., Zheng, J., and Wei, Z.: First mapping of polarization-dependent vegetation optical depth and soil moisture from SMAP L-band radiometry, Remote Sensing of Environment, 302, 113970, https://doi.org/10.1016/j.rse.2023.113970, 2024.

Rodell, M., Houser, P., Jambor, U. E. A., Gottschalck, J., Mitchell, K., Meng, J., Arsenault, K., Brian, C., Radakovich, J., Mg, B., Entin, J., Walker, J., Lohmann, D., and Dl, T.: The Global Land Data Assimilation System, bams, 85, 381-394, 10.1175/BAMS-85-3-381, 2004.

Rodríguez-Fernández, N. J., Mialon, A., Mermoz, S., Bouvet, A., Richaume, P., Al Bitar, A., Al-Yaari, A., Brandt, M., Kaminski, T., Le Toan, T., Kerr, Y. H., and Wigneron, J.-P.: An evaluation of SMOS L-band vegetation optical depth (L-VOD) data sets: high sensitivity of L-VOD to above-ground biomass in Africa, Biogeosciences, 15, 4627-4645, 10.5194/bg-15-4627-2018, 2018.

Rodriguez-Fernandez, N. J., Aires, F., Richaume, P., Kerr, Y. H., Prigent, C., Kolassa, J., Cabot, F., Jimenez, C., Mahmoodi, A., and Drusch, M.: Soil Moisture Retrieval Using Neural Networks: Application to SMOS, IEEE Transactions on Geoscience and Remote Sensing, 53, 5991-6007, 10.1109/tgrs.2015.2430845, 2015.

Saatchi, S. S., Harris, N. L., Brown, S., Lefsky, M., Mitchard, E. T., Salas, W., Zutta, B. R., Buermann, W., Lewis, S. L., Hagen, S., Petrova, S., White, L., Silman, M., and Morel, A.: Benchmark map of forest carbon stocks in tropical regions across three continents, Proc Natl Acad Sci U S A, 108, 9899-9904, 10.1073/pnas.1019576108, 2011.

Sadri, S., Pan, M., Wada, Y., Vergopolan, N., Sheffield, J., Famiglietti, J. S., Kerr, Y., and Wood, E.: A global near-real-time soil moisture index monitor for food security using integrated SMOS and SMAP, Remote Sensing of Environment, 246, 10.1016/j.rse.2020.111864, 2020.

Schmitt, A. U. and Kaleschke, L.: A Consistent Combination of Brightness Temperatures from SMOS and SMAP over Polar Oceans for Sea Ice Applications, Remote Sensing, 10, 10.3390/rs10040553, 2018.

Simard, M., Pinto, N., Fisher, J. B., and Baccini, A.: Mapping forest canopy height globally with spaceborne lidar, Journal of Geophysical Research, 116, 10.1029/2011jg001708, 2011.

Wagner, W., Naeimi, V., Scipal, K., de Jeu, R., and Martínez-Fernández, J.: Soil moisture from operational meteorological satellites, Hydrogeology Journal, 15, 121-131, 10.1007/s10040-006-0104-6, 2006.

Wagner, W., Hahn, S., Kidd, R., Melzer, T., Bartalis, Z., Hasenauer, S., Figa-Saldaña, J., de Rosnay, P., Jann, A., Schneider, S., Komma, J., Kubu, G., Brugger, K., Aubrecht, C., Züger, J., Gangkofner, U., Kienberger, S., Brocca, L., Wang, Y., Blöschl, G., Eitzinger, J., and Steinnocher, K.: The ASCAT Soil Moisture Product: A Review of its Specifications, Validation Results, and Emerging Applications, Meteorologische Zeitschrift, 22, 5-33, 10.1127/0941-2948/2013/0399, ·-··

Wang, H., Ciais, P., Sitch, S., Green, J. K., Tao, S., Fu, Z., Albergel, C., Bastos, A., Wang, M., Fawcett, D., Frappart, F., Li, X., Liu, X., Li, S., and Wigneron, J. P.: Anthropogenic disturbance exacerbates resilience loss in the Amazon rainforests, Glob Chang Biol, 30, e17006, 2024.

Wang, J. R. and Choudhury, B. J.: Remote sensing of soil moisture content, over bare field at 1.4 GHz frequency, Journal of Geophysical Research, 86, 10.1029/JC086iC06p05277, 1981.

Wigneron, J.-P., Li, X., Frappart, F., Fan, L., Al-Yaari, A., De Lannoy, G., Liu, X., Wang, M., Le Masson, E., and Moisy, C.: SMOS-IC data record of soil moisture and L-VOD: Historical development, applications and perspectives, Remote Sensing of Environment, 254, 10.1016/j.rse.2020.112238, 2021.

Wigneron, J.-P., Ciais, P., Li, X., Brandt, M., Canadell, J. G., Tian, F., Wang, H., Bastos, A., Fan, L., Gatica, G., Kashyap, R., Liu, X., Sitch, S., Tao, S., Xiao, X., Yang, H., Espinoza Villar, J. C., Frappart, F., Li, W., Qin, Y., De Truchis, A., and Fensholt, R.: Global carbon balance of the forest: satellite-based L-VOD results over the last decade, Frontiers in Remote Sensing, 5, 10.3389/frsen.2024.1338618, 2024.

Wigneron, J. P., Kerr, Y., Waldteufel, P., Saleh, K., Escorihuela, M. J., Richaume, P., Ferrazzoli, P., de Rosnay, P., Gurney, R., Calvet, J. C., Grant, J. P., Guglielmetti, M., Hornbuckle, B., Mätzler, C., Pellarin, T., and Schwank, M.: L-band Microwave Emission of the Biosphere (L-MEB) Model: Description and calibration against experimental data sets over crop fields, Remote Sensing of Environment, 107, 639-655, 10.1016/j.rse.2006.10.014, 2007.

Wigneron, J. P., Jackson, T. J., O'Neill, P., De Lannoy, G., de Rosnay, P., Walker, J. P., Ferrazzoli, P., Mironov, V., Bircher, S., Grant, J. P., Kurum, M., Schwank, M., Munoz-Sabater, J., Das, N., Royer, A., Al-Yaari, A., Al Bitar, A., Fernandez-Moran, R., Lawrence, H., Mialon, A., Parrens, M., Richaume, P., Delwart, S., and Kerr, Y.: Modelling the passive microwave signature from land surfaces: A review of recent results and application to the L-band SMOS & SMAP soil moisture retrieval algorithms, Remote Sensing of Environment, 192, 238-262, 10.1016/j.rse.2017.01.024, 2017.

Xing, Z., Li, X., Fan, L., Colliander, A., Frappart, F., de Rosnay, P., Fernandez-Moran, R., Liu, X., Wang, H., Zhao, L., and Wigneron, J.-P.: Assessment of 9 km SMAP soil moisture: Evidence of narrowing the gap between satellite retrievals and model-based reanalysis, Remote Sensing of Environment, 296, 10.1016/j.rse.2023.113721, 2023.

Xing, Z., Li, X., & Wigneron, J.-P. (2025). An operational global L-band soil moisture and vegetation optical depth dataset from optimized 40° SMOS brightness temperatures [Data set]. Zenodo. https://doi.org/10.5281/zenodo.17647385.

Xing, Z., Fan, L., Zhao, L., De Lannoy, G., Frappart, F., Peng, J., Li, X., Zeng, J., Al-Yaari, A., Yang, K., Zhao, T., Shi, J., Wang, M., Liu, X., Hu, G., Xiao, Y., Du, E., Li, R., Qiao, Y., Shi, J., Wen, J., Ma, M., and Wigneron, J.-P.: A first assessment of satellite and reanalysis estimates of surface and root-zone soil moisture over the permafrost region of Qinghai-Tibet Plateau, Remote Sensing of Environment, 265, 10.1016/j.rse.2021.112666, 2021.

Yi, C., Li, X., Zeng, J., Fan, L., Xie, Z., Gao, L., Xing, Z., Ma, H., Boudah, A., Zhou, H., Zhou, W., Sheng, Y., Dong, T., and Wigneron, J.-P.: Assessment of five SMAP soil moisture products using ISMN ground-based measurements over varied environmental conditions, Journal of Hydrology, 619, 10.1016/j.jhydrol.2023.129325, 2023.

Zhao, T., Shi, J., Entekhabi, D., Jackson, T. J., Hu, L., Peng, Z., Yao, P., Li, S., and Kang, C. S.: Retrievals of soil moisture and vegetation optical depth using a multi-channel collaborative algorithm, Remote Sensing of Environment, 257, 10.1016/j.rse.2021.112321, 2021.

Zotta, R.-M., Moesinger, L., van der Schalie, R., Vreugdenhil, M., Preimesberger, W., Frederikse, T., de Jeu, R., and Dorigo, W.: VODCA v2: multi-sensor, multi-frequency vegetation optical depth data for long-term canopy dynamics and biomass monitoring, Earth System Science Data, 16, 4573-4617, 10.5194/essd-16-4573-2024, 2024.